ACTA MATERIALIA TRANSYLVANICA

Material Sciences Publications

Volume 3, Issue 2

ERDÉLYI MÚZEUM-EGYESÜLET
Cluj-Napoca
2020

A folyóirat megjelenését támogatta a Magyar Tudományos Akadémia, a Bethlen Gábor Alapkezelő Zrt. és az EME Műszaki Tudományok Szakosztálya / The publication of this magazine was supported by the Hungarian Academy of Sciences, by the Bethlen Gábor Fund and by the TMS – Department of Engineering Sciences

Kiadó / Publisher: Erdélyi Múzeum-Egyesület
Felelős kiadó / Responsible publisher: Biró Annamária
Olvasószerkesztő / Proofreader: Szenkovics Enikő (magyar), David Speight (English)
Szerkesztőségi titkár / Editorial secretary: Kisfaludi-Bak Zsombor
Borítóterv / Cover: Könczey Elemér
Nyomdai munkálatok / Printed at: F&F International Kft., Gyergyószentmiklós

ISSN 2601-1883, ISSN-L 2601-1883
DOI: 10.33923/amt-2020-02
A folyóirat honlapja: https://www.eme.ro/publication-hu/acta-mat/mat-main.htm
The journal website: https://www.eme.ro/publication/acta-mat/mat-main.htm

Az *Acta Materialia Transylvanica. Anyagtudományi Közlemények* az Erdélyi Múzeum-Egyesület (EME) Műszaki Tudományok Szakosztályának folyóirata, amely az anyagtudományok területéről közöl tudományos közleményeket: szakcikkeket, összefoglalókat (szemléket), tanulmányokat. A folyóirat célja összképet adni kiemelten a Kárpát-medencei kutatási irányokról, tudományos eredményeiről, s ezt széles körben terjeszteni is. A folyóirat az EME felvállalt céljaihoz híven a magyar szaknyelv ápolását is támogatja, így a nyomtatott folyóirat magyar nyelven jelenik meg, mely az Erdélyi digitális adattárban elérhető (https://eda.eme.ro/handle/10598/30356). A széles körű nemzetközi terjesztés érdekében a folyóirat teljes angol nyelvű változatát is közzétesszük.

Acta Materiala Transylvanica – Material Sciences Publications – is a journal of the Technical Sciences Department of the Transylvanian Museum Society, publishing scientific papers, issues, reviews and studies in the field of material sciences. Its mission is to provide and disseminate a comprehensive picture focusing on research trends and scientific results in the Carpathian basin. In accordance with the general mission of the Transylvanian Museum Society it aims to support specialized literature in Hungarian. The printed version of the journal is published in Hungarian and is available in the Transylvanian Digital Database (https://eda.eme.ro/handle/ 10598/30356). However, we would like to spread it internationally, therefore the full content of the journal will also be available in English.

Tartalom / Content

sciendo

Acta Materialia Transylvanica 3/2. (2020) 61–64.
DOI: hungarian: https://doi.org/10.33923/amt-2020-02-01
english: https://doi.org/10.33924/amt-2020-02-01

ACTA MATERIALIA TRANSYLVANICA

Adhesion Behavior of PVD-coated Cutting Tools

Enikő Réka FÁBIÁN,[1] Richard HORVÁTH[2]

Óbuda University, Donát Bánki Faculty of Mechanical and Safety Engineering. Budapest, Hungary

[1] *fabian.reka@bgk.uni-obuda.hu*

[2] *horvath.richard@bgk.uni-obuda.hu*

Abstract

Cutting with TiAlN or CrAlN tip PVD-coated tungsten carbide-based inserts manufactured by powder metallurgy, we found no significant difference in the wear behavior of inserts regardless of whether the insert was used in wet or dry conditions. We determined the adhesion properties of the coating layers with a scratch test and by Daimler–Benz test. On the tungsten-based carbide cutting tool, the thinner TiAlN coating showed slightly better adhesion than the thicker CrAlN coating.

Keywords*: TiAlN, CrAlN, adhesion test, Calo test.*

1. Introduction

Cutting tools can be classified into different groups based on their material, geometrical shape, purpose and conditions of use. Based on their field of use, there are turning, drilling, milling and other tools. A tool has to fulfil the following requirements: high-quality cutting, precision, long life, productivity, and economical use. The tool can only fulfil these requirements if it has the necessary qualities. Of these, material properties are of paramount importance. An important cause of the failure of tools is wear due to abrasive and dynamic loads. Cutting tools are often surface treated [1–5], or coated [6–9], so that they are more resistant to wear. The properties of coatings depend on their structure, orientation, coefficient of friction but also on how much heat treatment the metal has received [10–11].

2. Previous research

According to literature sources, on tungsten-carbide tools, TiAlN suffers less wear than CrAlN coating [10], while on hot-forming tool steels, CrAlN coatings exhibit better adhesion resistance than TiAlN coatings [11]. We performed cutting on cast state GX2CrNiMoCuN25-6-3-3 quality super duplex steel in industrial conditions for 5 minutes. Cutting speed (v_c) was 70 m/min, feed (f) was 0.175 mm, and depth of cut (a) was 1 mm. We found that the wear of the two CNMG 120408 inserts with the two different coatings (nanocrystallite TiAlN and nanocrystallite CrAlN coating) was not considerably different regardless of whether cutting was performed in dry or lubricated conditions (Figure 1) Wear was present in both cases.

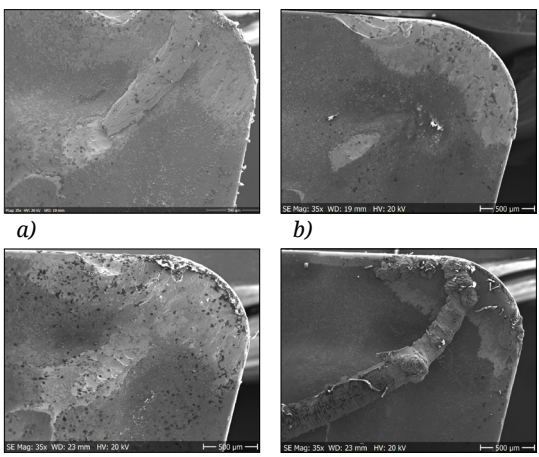

Figure 1. *Wear of coated cutting inserts. Built-up edge a) TiAlN coating + dry cutting; b) TiAlN coating + lubricated cutting; c) CrAlN coating + dry cutting; d) coating + lubricated cutting*

Figure 1 a) shows that after five minutes of dry cutting intact coating can only be found outside the "zone" of the depth of cut on the insert with the TiAlN coating. When lubricated cutting was performed, a built-up edge did not form on the rake surface up to the chip breaking groove on the TiAlN-coated insert, but the coating disappeared from the chip breaking groove and its immediate vicinity due to abrasive wear (**Figure 1 b**). Similarly to dry cutting, lubricated cutting also caused edge breakoff along the main cutting edge.

On the CrAlN-coated tool there were no shavings or built-up edge in the chip breaking zone of the rake surface, but the continuous wear of the chips completely wore off the coating (**Figure 1 c**). During lubricated cutting, there was no edge breakoff on the CrAlN-coated tool, but many built-up edges of the duplex steel can be seen along the edge. On this tool, the built-up edge from the duplex steel can be found on the rake surface, over a long distance, even in the chip breaking zone (**Figure 1 d**).

The test results were somewhat surprising because according to the distributor, the coefficient of friction of CrAlN is lower (0.4) than that of the TiAlN coating (0.6); the hardness of the TiAlN coating is 3200 HV, while that of the CrAlN coating is 3300 HV.

To find out why the coated inserts behaved as they did, we examined the actual thickness of the coating and its adhesion with various methods.

3. Materials and methods

The CNMG120408 inserts were manufactured by powder metallurgy. They were coated in conventional industrial conditions. Since not only the coating but the inserts are very hard too, the measurement of layer thickness with metallographic methods is very complicated; a coating is likely to break off, even when cut with a diamond disk. The hardness of the material makes conventional metallographic sanding complicated too, therefore we measured layer thickness with the Calo test **[12–14]** using a 30 mm diameter Al_2O_3 abrasion ball. The test is based on the wear between two surfaces based on abrasion. In the test, a Ø30 mm ball was coated with a suspension containing abrasive particles. The ball was then rotated through friction drive and pushed against the surface to be tested.

For the adhesion test, we used scratch test with MST³ equipment, **[15]**, and Daimler–Benz test **[16]**.

4. Results

During the Calo test, the abrasion ball with the abrasive suspension creates a crater, with the shape of a spherical cap (**Figure 2**). The wear mark is measured under a microscope and the layer thicknesses are calculated **[14]**.

Layer thickness (T) is calculated as follows:

$$T = \frac{X \cdot Y}{D};\ \mu m \qquad (1)$$

Notation can be found in **Figure 2.**

On the coated inserts, the thickness of the different coatings is different. (**Figure 3**).

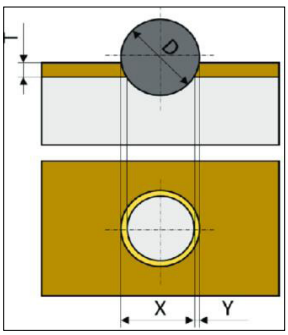

Figure 2. *Notation for calculating layer thickness.*

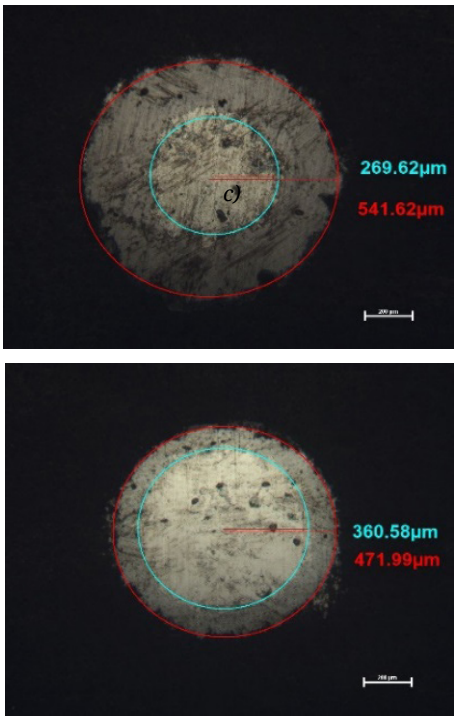

a)

b)

Figure 3. *Images of measuring the thickness of coating layers on CNMG120408 inserts a) TiAlN coating b) CrAlN coating.*

After the Calo test, we measured the circles around the spherical caps with an optical microscope and calculated the layer thicknesses. The thickness of the TiAlN layer was 6.2–7.4 µm on average, while the CrAlN layer just exceeded 3 µm (3.3 µm on average).

The results of the scratch tests performed with the MST^3 device are shown in **Figure 4.**

During the scratch test of the inserts, the flaking of the CrAlN layer has already started at a force of 4.03 N, while the TiAlN coating did not exhibit characteristic chipping at a fine scale low load even at the maximum load of 30 N that can be applied by the device. However, acoustic signals were detected even at very small loads.

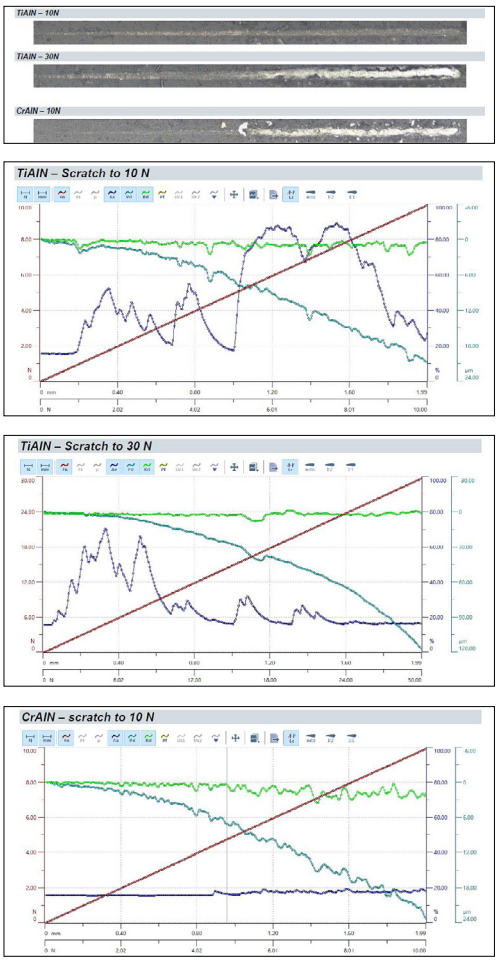

Figure 4. *The results of the scratch test*
a) the optical representation of scratches on the CNMG 120408 coated inserts
b) TiAlN coating, max load 10 N
c) TiAlN coating, max load 300 N
d) CrAlN coating, max load 10 N

For the Daimler–Benz test, a Rockwell hardness tester with a diamond cone indenter and a load of 1470 N was used.

Daimler–Benz test was evaluated using an optical microscope as can be seen at **Figures 5.** The imprints were classified from HF1 to HF6 conforming to VDI 3198 **[16]**. The adhesion of the CrAlN layer (produced by PVD) on the CNMG 120408 inserts shows rather poor adhesion (H5/H6 based on the series of images), while the TiAlN layers have somewhat better adhesion, they receive a classification of H3/H4 based on the Daimler–Benz test, as **Figure 5** indicates.

5.Conclusions

The adhesion tests explain the relatively fast wear of the coating during cutting both in dry and lubricated conditions. The tests show that the relatively thick TiAlN coating produces acceptable adhesion on the CNMG120408 inserts, which are produced by powder metallurgy and have a relatively rough surface. On the other hand, the CrAlN coating breaks up as a result of even a small force and is classified as rather bad by the Daimler–Benz test.

Acknowledgements

The authors wish to express their thanks for the financial support in the framework of the EFOP-3.6.1-16-2016-00010 project to the Hungarian State and the European Union.

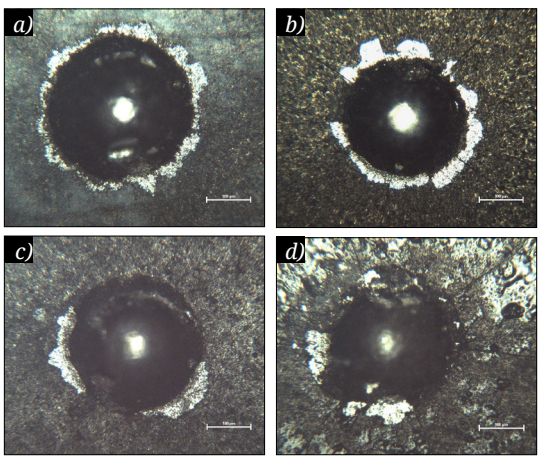

Figure 5. *The results of the Daimler–Benz tests at CNMG 120408 coated inserts*
a) TiAlN coating on insert 1
b) TiAlN coating on insert 2
c) CrAlN coating on insert 1
d) CrAlN coating on insert 2

References

[1] Bitay E.: *Bevonatolt gyorsacélok kopásállósága/ Coated HS Steels Wear Resistance.* XVIII. FMTÜ, EME, Kolozsvár, Románia 2013, 73–76. https://doi.org/10.36243/fmtu-2013.10

[2] Kovács T. A., Umesh Mhatre, Nyikes Z., Bitay E.: *Surface Modification Innovation for Wear Resistance Increasing*. In: IOP Conf. Series: Materials Science and Engineering. vol. 613. (2019). 5th International Conference on Competitive Materials and Technology Processes 8–12 October 2018, Miskolc-Lillafüred, Hungary. https://doi.org/10.1088/1757-899X/613/1/012039

[3] Fábián E. R, Furkó M., Vehoczki B.: *Különböző típusú elektrokémiai bevonatok tulajdonságai*. In: Fiatal Műszakiak Tudományos Ülésszaka, 19. (2014) 145–148. https://doi.org/10.36243/fmtu-2014.029

[4] Kovács-Coskun T., Bitay E.: *The hardness control in the coated surface layer*. Materials Science Forum, 729. (2013) 415–418. https://doi.org/10.4028/www.scientific.net/MSF.729.415

[5] Bitay E., Kovács T.: *The effect of the laser surface treatments on the wear resistance*. Materials Science Forum, 649. (2010) 107–112. https://doi.org/10.4028/www.scientific.net/MSF.649.107

[6] Bitay E.: *Lézeres felületkezelés és modellezés.* Műszaki Tudományos Füzetek 4., EME, Kolozsvár, 2007. https://doi.org/10.36242/mtf-04

[7] Bagyinszky Gy., Bitay E.: *Kopásálló felületkezelt rétegek minősítése/Characterization of surface treated, wear resistant layers*. In: Fiatal Műszakiak Tudományos Ülésszaka, 14. (2009) 13–16. https://doi.org/10.36243/fmtu-2009.08

[8] Bitay E.: *Lézeresen kezelt felületek kopásállósága.* In: Fiatal Műszakiak Tudományos Ülésszaka, 6. (2001) 111–118. https://doi.org/10.36243/fmtu-2001.23

[9] Sebestyén A., Nagyné Halász E., Bagyinszky Gy., Bitay E.: *Felületmódosítási eljárások hatása acélok kopásállóságára.* In: Fiatal Műszakiak Tudományos Ülésszaka, 12. (2007) 161–169. https://doi.org/10.36243/fmtu-2007.4

[10] Liu Aihua, Deng Jianxin, Cui Haibing, Chen Yangyang, Zhao Jun: *Friction and wear properties of TiN, TiAlN, AlTiN and CrAlN PVD nitride coatings.* Int. Journal of Refractory Metals and Hard Materials, 31. (2012) 82–88.

[11] Tillmann W., Grisales D., Stangier D., Butzke T.: *Tribomechanical behaviour of TiAlN and CrAlN coating deposited onto AISI H11 with different heat treatments*. Coating, 9/519. (2019) 2–21.

[12] Rupetsov V., Minchev R.: *Experimental calo tester for the coating thickness measurement.* 15th International Scientific Conference Smolyan, Bulgaria, 2016. 188–191.

[13] Tribotechnik: *Kemény bevonati rétegek vastagságmérése Calo-teszttel* https://www.tribotechnic.com/en/products/calotest/

[14] PVD-bevonatok vastagságmérése https://www.pvd-coatings.co.uk/Ph.D.-coating-technology/testing-equipment/coating-thickness-tester

[15] Bevonatok tapadásvizsgálata karcteszteléssel https://www.anton-paar.com/corp-en/products/details/micro-scratch-tester-mst3

[16] Verein-Deutscher-Ingenieure 1992 Daimler Benz Adhesion Test VDI 3198. Dusseldorf, VDI-Verlag 7.

sciendo

Acta Materialia Transylvanica 3/2. (2020) 65–69.
DOI: hungarian: https://doi.org/10.33923/amt-2020-02-02
english: https://doi.org/10.33924/amt-2020-02-02

ACTA MATERIALIA TRANSYLVANICA

Finite Element Analysis of Size Effect for Forming-Limit Curves

Viktor GÁL

University of Miskolc, Institute of Material Engineering and Materials Technology Miskolc, Hungary, metgv@uni-miskolc.hu

Abstract

Nowadays, finite element (FE) methods are widely used for the analysis of Body in White parts production. An FE software applies the forming-limit diagram to predict the failure of the sheet metal. There are many new materials for weight reduction; for these new materials, the determination of forming-limit curves (FLC) is important to studying formability issues. There are some cases where the available material for the measurements is not enough or due to some specific measurement parameter, the standard test specimen cannot be used. In these cases, the geometry of the test pieces and the testing equipment should be reduced. In this paper, the material card for DC05 (1.0312) steel was determined based on a tensile test and the Nakajima test. With the material card, simulations were performed to investigate the size effect of the hemispherical punch used for Nakajima forming method. Based on the simulations, the difference between the FLC-s (determined with different equipment) was found to be negligible.

Keywords*: FLC, size effect, forming-limit curve.*

1. Introduction

In recent years, development trends in the automotive industry have been determined by the reduction of harmful emissions. These aspirations can be realized by reducing the weight of automobiles. In order to decrease the weight of vehicles, it is not enough to simply reduce the amount of the applied materials; it is also necessary to increase their strength to fulfil safety requirements. As a result, nowadays, new high-strength materials such as boron alloyed manganese steels (e.g. 22MnB5), or high-strength aluminium alloys (AA7075) and related technologies (Press Hardening, Hot Forming and Quenching) [1] have been developed.

Nowadays, computer-aided design of sheet metal parts and finite element modelling of the technological processes are involved in the everyday practice. Accordingly, the software needs to have the possibility for applying the new materials and also the new technologies. For a simulation that adequately predicts the physical process, the behaviour of a material needs to be determined by the appropriate constituent equations. For sheet metals these are the flow curves, which show how the material responds to plastic deformation, the yield-surfaces defining the limit of elastic deformation, and the Forming Limit Diagram (FLD). The FLD describes the limits of formability in the coordinate system of major and minor principal strains. These three properties of the sheet metal are collected in the so-called material cards.

Defining the behaviour of the material for conventional (cold) forming processes can be regarded as common practice. However, the high-strength materials - mentioned above - typically are formed by hot-forming technologies [2]. Nowadays, computer-aided design of sheet metal parts and finite element modelling of the technological processes are involved in the everyday practice. Accordingly, the software needs to have the possibility for applying the new materials and also the new technologies. For a simulation that adequately predicts the physical process, the behaviour of a material needs to be determined by the appropriate constituent equations. For sheet metals these are the flow curves, which show how the material responds to plastic deformation, the

yield-surfaces defining the limit of elastic deformation, and the Forming Limit Diagram (FLD). The FLD describes the limits of formability in the coordinate system of major and minor principal strains. These three properties of the sheet metal are collected in the so-called material cards.

Defining the behaviour of the material for conventional (cold) forming processes can be regarded as common practice. However, the high-strength materials - mentioned above - typically are formed by hot-forming technologies [2]. In hot forming processes, the behaviour of the material is primarily determined by its dependence on temperature and strain rate, which clearly induces a change in the constitutive equations describing it. Dependence on these parameters makes the determination of material properties significantly more difficult.

Thus, in the case of hot forming, it is necessary to set up an experimental matrix to properly describe the deformation of the material where there are varying strain rates at different temperatures or different temperatures at a given strain rate. The increase in the number of tests makes it clear that material card for the hot forming simulation requires a larger amount of specimen than in cold forming. For newly developed materials, it is not always possible to produce large amounts of standardized size specimens that are typically required for testing, especially for a forming limit diagram.

Determining the FLC using the conventional Nakajima test causes considerable difficulties in a hot forming environment. In this case, in order to meet the requirements of the aforementioned experimental matrix in terms of temperature and strain rate, an equipment for FLD determination has been developed (**Figure 1**) that can be used with the GLEEBLE 3500 thermo-mechanical simulator at the Institute of Materials Engineering and Materials Technology, University of Miskolc, Hungary. This new device is a proportionally reduced equivalent to the tooling required for the standard Nakajima test.

The basic concept behind the tests presented in this paper is the well-known fact that in the case of the FLC tests performed in the equipment manufactured according to ISO 12004 standard **[3],** the positioning of the forming limit diagram changes in the coordinate system of the principal strains if the sheet thickness changes. This effect is more significant on the right side of the FLD ($\varepsilon_2 > 0$) but it is valid that increasing the sheet thickness the FLC will be shifted upwards along the ε_1 axis **[4]** (**Figure 2**).

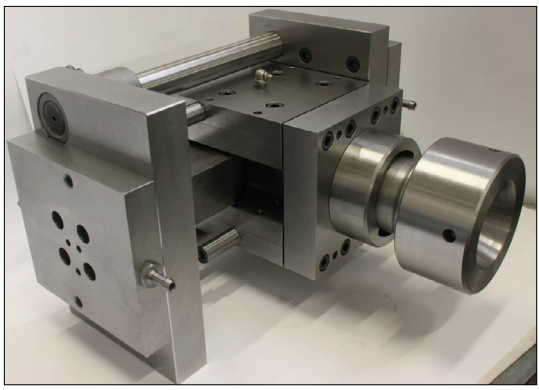

Figure 1. *Proportionally reduced equipment for determining FLD.*

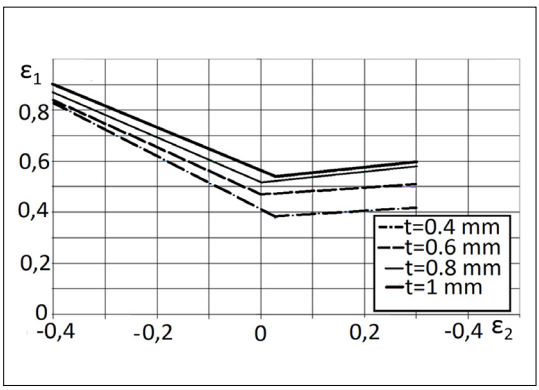

Figure 2. *Effect of sheet thickness on the forming limit curves for DC05(1.0312) material grade.* **[4]**

Thus, if we change the sheet thickness to punch diameter ratio, the position of the FLC in the coordinate system of the major deformations will change. In this paper, further experiments were performed to investigate the effect of punch diameter / sheet thickness ratio on the forming limit curve (FLC). In these experiments, the influence of the quotient on the FLC was tested by changing the diameter of the equipment rather than modifying the thickness of the sheet.

2. Material testing

As mentioned above, the basic prerequisite for accurate finite element modelling is the determination of a material card that precisely describes the deformation. For sheet metal parts, this can be achieved by performing the tensile test and the Nakajima test. The material quality to be tested was 1.4828 austenitic stainless steel with 1 mm sheet thickness, which is typically used for parts in exhaust systems.

The material was first cut by laser cutting process for performing tensile tests in three different directions i.e. in the rolling direction, 45 degrees and perpendicular to it. The tensile test was performed with an MTS universal electro-hydraulic device at the Institute of Materials Engineering and Materials Technology, University of Miskolc, Hungary. In addition to the longitudinal and transverse size change of the specimens, the corresponding force values were continuously recorded. By converting the values of force and changes in length, true stress and true strain values are determined. Further, the yield curve was determined from the section of these values within the range of plastic deformation.

The onset of plastic deformation of the material in the main stress plane σ_I–σ_{II} is determined by an origin-centred ellipse, i.e. the yield surface. The yield surface varies continuously as a function of deformation, which can be derived from the flow curve. In order to integrate the yield surface later into the software, the plastic anisotropy coefficients describing the direction dependence of the sheet rolling is also determined from the records of tensile tests.

The third part of the material card used in finite element modelling is the Forming Limit Diagram, and more specifically the Forming Limit Curve (FLC) itself, which is the curve connecting the points of fracture in the coordinate system of major strains. To obtain the FLC basically five (**Figure 3**), but a minimum of three specimens of different bridge widths are required. The specimens of different bridge widths were laser cut, as mentioned for the tensile test, and were machined from a 1 mm sheet. During the experiments, the test specimens were fixed temporarily between a die and a blank-holder to avoid any movement, and then loaded with a hemispherical punch in the direction of the sheet thickness until cracking occurred. During loading, the displacement of the points of the 1 mm quadrilateral mesh applied to the surface of the specimens was continuously recorded by a four-camera optical measuring system.

The displacement of the mesh points relative to one another is automatically converted by the measuring system into a deformation, thanks to the continuous recording, which provided the accurate picture of the entire process of deformation. The FLC was determined based on the deformations associated with the fracture.

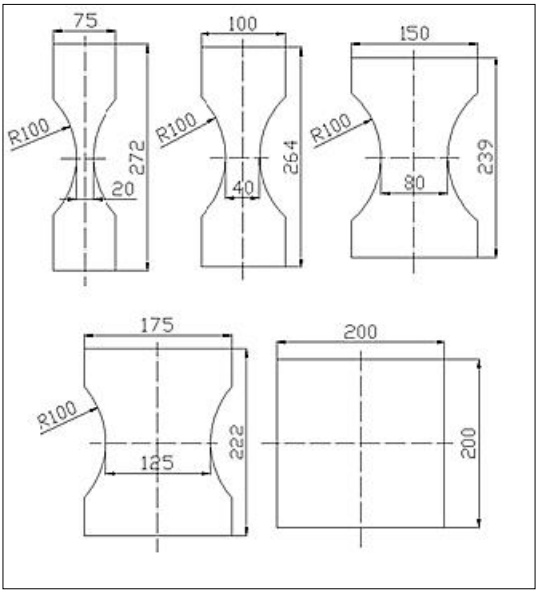

Figure 3. *Specimen geometries with different bridge widths for determining FLD-s.*

3. Finite element modelling

After performing the physical measurements, finite element modelling was used to investigate the effect of deviation from the standardized tooling. The simulations were performed in AutoForm R8 software, where first the material card **[5]**, and then the tooling was defined.

AutoForm provides the ability to import into the software the points defined in the previous section for each deformation characteristic. A drawback of the flow curve determination with the tensile test is that the points thus obtained cover only a small range of deformation. To overcome this problem, the software performs extrapolation using a mathematical function added to specific points. Several known mathematical models are available for extending the physical points of the flow curve; in this case, we applied a combined Swift and Hockett-Sherby approximation widely used in the field of sheet metal forming, which uses the mathematical form as described in equation (1). In this equation ε_{pl} and ε_0 are strains, σ_{sat} and σ_i are stresses, a and m are exponents in the strain hardening law.

$$\sigma = (1-\alpha)\left[C\cdot(\varepsilon_{pl}+\varepsilon_0)^m\right]+\alpha\left[\sigma_{sat}-(\sigma_{sat}-\sigma_i)e^{a\cdot\varepsilon_{pl}^p}\right] \quad (1)$$

To describe the yield surface, the Hill48 model was selected for which the anisotropy coefficient value was derived from the tensile tests.

Once the material card was defined, the appropriate tool geometries were imported. The standardized tooling model is illustrated in **Figure 4,** where the punch diameter marked D_b was 100 mm. In order to examine the size effect, it was necessary to reduce the diameter of the stamp, so that the diameter of 100 mm was first reduced by half and then by one-fifth, so that all other dimensions of the test equipment were reduced proportionally.

After the FE modelling of the equipment was completed, the first necessary step was to determine the parameters of the simulation. Friction also influences the location of rupture (particularly in the region of positive deformation on the FLD) as well as the deformation path of the specimen **[6]**. In order to get appropriate results, the friction parameter was set for the largest bridge width piece with standard-shaped tools, because of the large contact areas, which is the most important factor to consider in this case.

After defining the characteristic friction coefficient, simulations were performed for the next four bridge widths with the given settings. In the evaluation, the physical thickness measurement of the maximum thickness at rupture was taken as the basis of the physical measurement and the main deformation was determined at this FE node.

The deformation points for the fracture thus obtained are illustrated in **Figure 5.** On the basis of these results, it can be stated that the FLC achieved by physical measurement and finite element modelling shows a good correlation.

Since the simulations on the 100 mm diameter punch are considered correct, it is further continued to compile the simulations for the proportionally reduced 50 mm and 20 mm stamps. It is also important to note that in these cases the geometry of the specimens shown in **Figure 3,** is reduced proportionally to the given diameter at constant plate thickness.

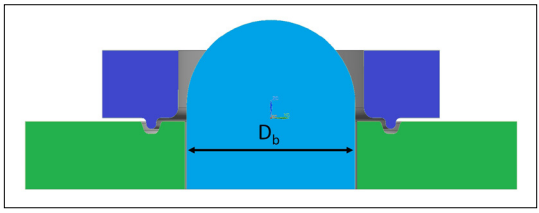

Figure 4. *Standardized tool geometry.*

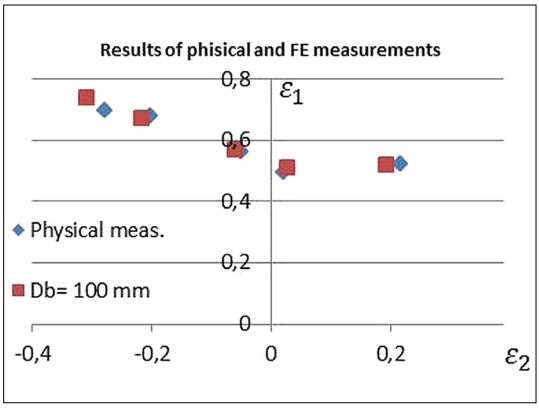

Figure 5. *Comparison the FLC points of the simulation and the physical measurement.*

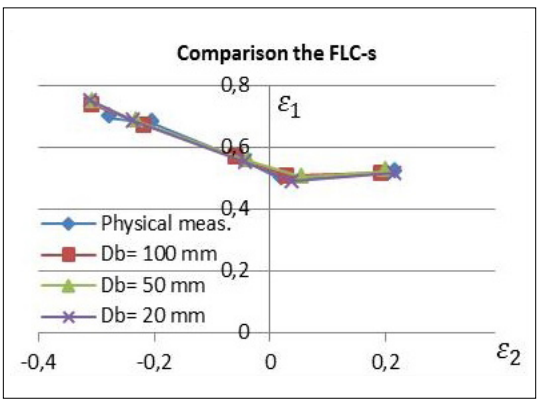

Figure 6. *Results of the size effect created by diameter change of hemispherical punch.*

4. Results and discussion

After running the simulations, the deformation of each specimen was evaluated for each of the three punch diameters. The strain distribution is the same for each bridge width. Calculating the fracture points was based on the sheet thickness measured at the 100 mm diameter punch and the strain in the thickness direction. The FLC-s for each punch diameter are illustrated in **Figure 6.**

From the corresponding correlation of the curves in **Figure 6** it can be stated that if the size of the punch is reduced proportionally, the FLD is not affected by the dimensional change at a given sheet thickness. So the punch diameter to sheet thickness ratio has no effect on the Forming Limit Curves, but only the sheet thickness.

Acknowledgments

The described article/presentation/study was carried out as part of the EFOP-3.6.1-16-2016-00011 “Younger and Renewing University – Innovative Knowledge

City – institutional development of the University of Miskolc aiming at intelligent specialisation" project implemented in the framework of the Szechenyi 2020 program. The realization of this project is supported by the European Union, co-financed by the European Social Fund.

References

[1] Tisza M., Czinege I.: *Comparative study of the application of automotive parts*. International Journal of Lightweight Materials and Manufacture, 1/4. (2018) 229–238. https://doi.org/10.1016/j.ijlmm.2018.09.001

[2] Tisza M.: *Nagyszilárdságú bóros mangán acélok autóipari alkalmazása*. Anyagmérnöki Tudományok, 39/1. (2016) 68–81.

[3] EN ISO 12004-2 Metallic materials – Sheet and strip – Determination of forming limit curves — Part 2: Determination of forming limit curves in laboratory 2006.

[4] Tisza M., Kovács P. Z.: *New methods for predicting the formability of sheet metals*. Production Processes and Systems, 5/1. (2012) 45–54.

[5] Tisza M., Lukács Zs., Kovács P. Z., Budai D.: *Some recent developments in sheet metal forming for production of lightweight automotive parts*. 36th IDDRG Conference – Materials Modelling and Testing for Sheet Metal Forming, Munich, Germany, Journal of Physics: Conf. Series 896 (2017) 012087. https://doi.org/10.1088/1742-6596/869/1/012087

[6] Kovács P. Z.: *Alakítási határdiagramok elméleti és kísérleti elemzése*. PhD-értekezés; Miskolc, 2012. https://doi.org/10.14750/ME.2013.030

sciendo

Acta Materialia Transylvanica 3/2. (2020) 70–75.
DOI: hungarian: https://doi.org/10.33923/amt-2020-02-03
english: https://doi.org/10.33924/amt-2020-02-03

ACTA MATERIALIA TRANSYLVANICA

Development Options for Coronary Stent Coatings

Izabella IZSÓ,[1] Lilla ASZTALOS[2]

Budapest University of Technology and Economics, Faculty of Mechanical Engineering, Department of Materials Science and Engineering

[1] *izso.izabella@gmail.com*

[2] *lilla@eik.bme.hu*

Abstract

In our research we investigated the effect of different surface qualities on the adhesion of polylactic acid coating on 316L steel. During the study, samples were electropolished and surface treated with aqua regia and Vilella reagent, and the coating was applied by dipping technology using a Yaskawa robot arm. Tribology tests were carried out to determine the adhesion, in addition to the force and friction conditions, the coating damage resulting from the measurements was also recorded. In addition to the coating adhesion assay, contact angle measurements were also performed. Based on our measurement results, it was found that compared to the three different surface treatment methods, the surface of the samples treated with Villella was more adherent to the polymer than to the conventional electropolished surface. In this case, the frictional force was also much lower than that of the polished specimens, therefore this surface treatment method may be suitable for improving the adhesion of the coating.

Keywords*: coronary stent, surface treatment, coating adhesion, PLA.*

1. Introduction

Coatings were initially used to enhance the biocompatibility of stents, but nowadays their primary goal is the controlled delivery of drugs used to inhibit neointimal hyperplasia. Regarding the optimal stent coating, the literature highlights three main aspects. The first and one of the most important factors is that the coating must be done on a dirt-free metal surface. Second, the surface roughness should be minimal relative to the thickness of the coating to ensure good uniformity and adhesion of the film layer. Furthermore, finally, the coating must be stable both when applied to the stent and after implantation. [1, 2]

The three drugs studied for the treatment of restenosis are heparin, sirolimus, and paclitaxel. Heparin was effective in reducing both thrombosis and neointimal proliferation, while sirolimus and paclitaxel were mainly used in their antiproliferative effects to block neointimal hyperplasia. [3, 4]

Proper surface treatment plays an important role in the design and manufacture of a stent. Roughening of the surface may increase the adhesion of the coating, but a surface that is too rough tends to thrombogenicity. A typical surface treatment method for stent types used in clinical practice is electropolishing. [5, 6]

In our previous research, we observed that the coating may detach from the surface of the stent already during implantation, due to the fact that the plastic coating carrying the drug does not adhere properly to the surface of the metal frame of the support. [7] The aim of the present research is to develop a surface treatment method to improve the adhesion of the polylactic acid coating on 316L type austenitic stainless steel, taking into account previous experience [8].

2. Methods

For the research, 30×30×0.3 mm, 316L type, austenitic stainless steel inserts were used. 5 specimens were electropolished, 5 specimens in aqua regia (20 mL methanol, 15 mL 65 % HNO_3, 45 mL 37 % HCl, up to 60 s, without power source), and 5 in Vilella reagent (200 mL ethanol, 2 g picric

acid, 10 mL of 37 % HCl, up to 60s, at 5V). Surface treatments were performed at 30 ± 1 °C. Furthermore, the samples were cleaned with acetone and ethanol according to the pre-programmed values in the robot before and after the surface modification, and then allowed to dry (3× acetone and 3× ethanol purification, respectively).

2.1. Electropolishing

Of the various surface treatment methods, electropolishing is one of the most popular surface modification methods due to its many advantages. One of these is that it can be performed on complex shapes, such as coronary stents of different shapes and geometries. It can be used to create a well-passivated, smooth, even and clean surface. During the polishing process, the metal is oxidized on the surface of the anode, causing the ions to dissolve into the electrolyte solution and then migrate to the cathode where they are reduced to form hydrogen. The electropolishing process is influenced by a number of parameters. Such parameters include anodic current density, applied potential, electrolyte temperature, polishing time, electrolyte composition and concentration, mixing method, and anode-cathode surface ratio. [9-12] Based on this research and our experience, electropolishing was performed at 5 V and 0.01 A/mm^2 in room temperature solution (25±1 °C) with ultrasonic vibration, phosphoric acid (H3PO4), sulfuric acid (H_2SO_4) and distilled water. It was performed in a 6:3:1 mixture to which 20 mL of glycerol was mixed. The polishing time was 3 minutes. (Figure 1).

2.2. Chemical etching

Electropolishing can create a very smooth surface, but the adhesion of the coating can be aided by roughening the surface by chemical etching. Similar experiments have already been carried out in the development of polyurethane coatings, in which it has already been demonstrated that the smaller the roughness of the stent surface, the easier it is for the coating to peel off. [13] However, polyurethane is no longer a typical drug carrier in medical technology, so taking into account the research and development trends, the present research examines the adhesion of polylactic acid.

Roughening of the surface was solved by chemical etching. In order to make the process repeatable, the process was automated with a robot arm (Yaskawa You teach me). The milling agent was stirred continuously with a magnetic stirrer (IKA RCT basic) at 30±1 °C. The duration of the surface treatment was 60 seconds, during which the robot arm moved the specimen in a circular manner in the solution (Figure 2).

Figure 1. *Electropolishing process.*

Figure 2. *Surface treatment with a Yaskawa „You teach me" robotic arm.*

2.3. Coating process

The coating was also applied to the surface-treated tiles automated with the robotic arm. The polylactic acid was dissolved in chloroform. The dipping time was 10 seconds, and after extraction, the coating formed on the tile was dried by rotating it along its axis.

2.4. Qualification of the coatings

The weight of the tiles was measured before, after and after the surface treatments. The effectiveness of the surface treatment was examined by electron microscopy (Zeiss EVO MA 10) and confocal microscopy (Sensofar, neox PLu). Surface roughness was also measured on reference, surface-treated and coated samples. The adhesion of the coating was evaluated by a tribological test (High Temperature Tribometer - CSM Switzerland). As the moisture-binding effect of a given plastic is important in medical technology, we also performed edge angle measurements as part of the research.

3. Results

3.1. Microstructure examination

The surface treatment methods used resulted in different surface morphologies, the scanning electron micrograph (SEM) of which is shown in Figures 3–5. Electropolishing, as expected, gave a smooth surface, while for samples milled with Vilella and aqua regia, the surface roughening was achieved. Each of the surfaces obtained after the treatments may be suitable for applying the polymer coating of our choice.

3.2. Weight measurement

The largest weight loss was caused by the electropolishing process (6–8 %), followed by the weight loss caused by aqua regia (0.5–1 %) and Vilella etchant (0.2–0.3 %).

After coating preparation, the weight of the inserts increased uniformly by 6 to 7 mg, which supports the success of the automation of the coating.

3.3. Surface roughness

Surface roughness was determined by confocal microscopy (Neox Flu, Sensofar). The surface roughness of the samples etched in the royal water was the highest, of the treated samples only the roughness less than the reference value was measured on the electropolished specimen (Table 1).

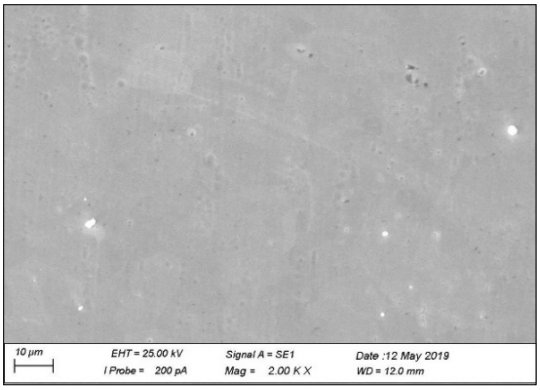

Figure 3. *Electron microscopic images of the surface of the electropolished 316L sheet.*

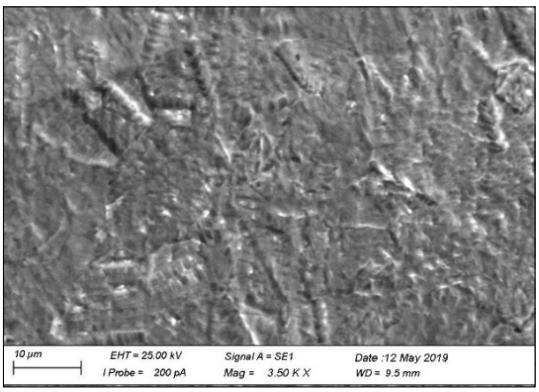

Figure 4. *Electron microscopic images of the surface of the aqua regia etched 316L sheet.*

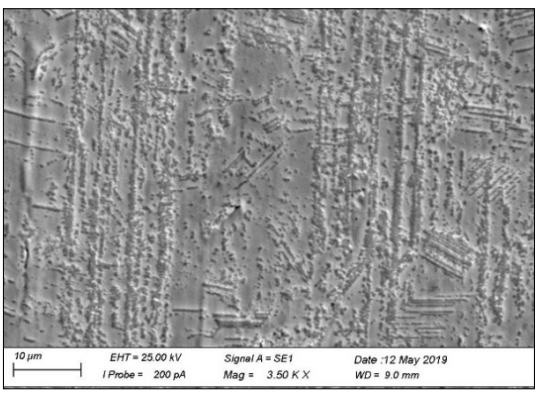

Figure 5. *Electron microscopic images of the surface of the Vilella etched 316L sheet.*

The values after coating preparation are summarized in Table 2. After coating, the average surface roughness of each sample decreased, which is advantageous because the low surface roughness during implantation reduces the force required to push the implant intravascularly.

Table 1. *Surface roughness measured on the samples (Sa = average of the deviations). The shown values are the average values of the 5 samples.*

Sample	Sa (µm)
Aqua regia etched	5.12
Vilella etched	4.53
Electropolished	2.66
Reference	2.73

Table 2. *Surface roughness measured on the samples after the coating process (Sa = average of the deviations). The shown values are the average values of the 4 samples.*

Sample	Sa (µm)
Aqua regia etched	1.33
Vilella etched	1.37
Electropolished	1.53
Reference	1.30

3.4. Coating thickness

The thickness of the coating was also determined by confocal microscopy. To this end, samples were selected from all types in which a part of the coating was mechanically removed from half of the coated section so that neither the raw material nor the remaining coating section was damaged; partial layer thickness could not be measured properly at the original boundary, as it would show a gradual thinning. By examining the total length of the boundary section thus formed (marked in yellow in **Figure 6**), the coating thickness is obtained by calculating the difference between the average level of the sample surface (green area in **Figure 6**) and the average coating thickness level (orange area in **Figure 6**). Unfortunately, the robotic arm method we currently use did not allow the samples to be dipped in their full length into the polymer, as the chuck would have been immersed together with the sample in the plastic solution. The polylactic acid coating would solidify on the chuck and insert together, and even the coating on the insert would be damaged as the chuck was removed. In the future, our goal is to further develop the current method in such a way that we are able to immerse the samples in polylactic acid along their entire length so that the layer thickness is as uniform as possible over the entire length of the sample.

The software of the applied confocal microscope made it possible to determine the exact height

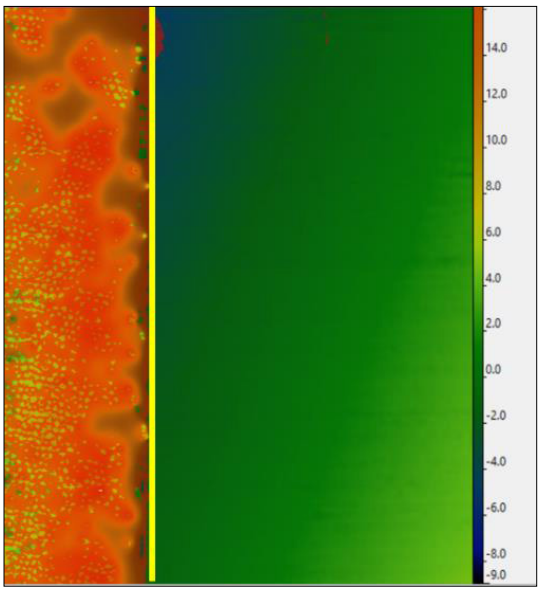

Figure 6. *Colour scale for determining layer thickness. The border section created during the incision is marked in yellow. The scale on the right shows the depth and height of the levels for each colour in µm.*

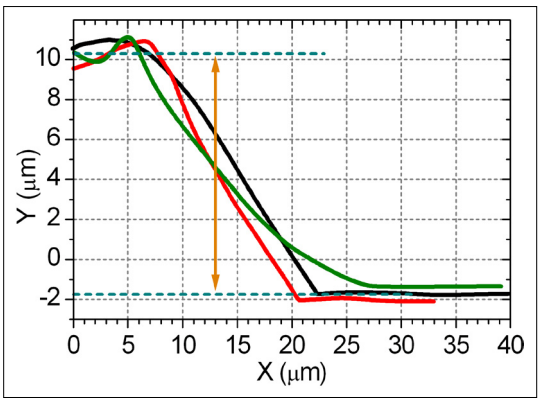

Figure 7. *Results of measurements with confocal microscopy; the yellow arrow-line shows the layer thickness.*

and depth values at the selected points as well as along the lines, in addition to the colour map representation. **Figure 7** shows the values of 3 line analysis. The measurement lines were recorded in a direction perpendicular to the boundary line. The average height of the coating layer as well as the average height of the plane of the plate were determined, and the thickness of the coating was obtained from the difference between the two. Based on the results, the average thickness of the coating prepared by us is 10.45 µm, which meets

the values of the literature and is almost identical to the typical coating thickness of the stents currently on the market.

3.5. Qualification of coating adhesion

The adhesion quality of the coating was determined by tribological testing, for which we used the High Temperature Tribometer CSM THT instrument in the laboratories of PROMATECH in Kosice. During the test, using the same load force, in our case 50 N, a needle on a disc was moved circularly on the surface of the insert. A detail of the "ditch" formed by the needle is shown in **Figure 8**.

Based on the experiment, we found that under the effect of the same loading force, the trench with the smallest depth (8.76 µm) was formed in the case of the samples treated with Vilella. Based on this, it can be said that the applied polymer coating was here the most resistant to the same load. In this case, the needle did not even reach the boundary of the metallic material of the sample, based on an average coating thickness of 10.45 µm. In contrast, there was a deeper difference beyond the coating thickness for the aqua regia-treated (17.5 µm) and electro polished (16.9 µm) samples. The deepest scratch depth (35.2 µm) was obtained for untreated but polymer-coated samples, i.e. it was the least "resistant" to the same load.

3.6. Edge angle

When measuring the edge angle, the wettability of the inserts was examined. From the data, we can deduce whether the blood wets the surface or not. This is important because the hydrophobic or hydrophilic nature of the surface can affect the effect of the coating on restenosis. Smaller flange angles means better wetting (minimum 0°), while larger flange angles (maximum 180°) can mean worse wetting. At a flange angle of less than 90°, it is said that the liquid wets the solid surface of the substrate, and at flange angles greater than 90°, we speak of non-wetting. Our measurement results are summarized in **Figure 9**.

From **Figure 9**, it can be seen that the polymer applied to the surface of the Vilella-treated samples has a wettability above 90°, i.e. the coating is more hydrophobic, even in the case of electropolished samples only. From this we can conclude that the blood wets the surface of our polymer less. This is good because it will cause the platelets, to stick less to the wall of the ‚foreign' substance and thus be less likely to cause thrombosis.

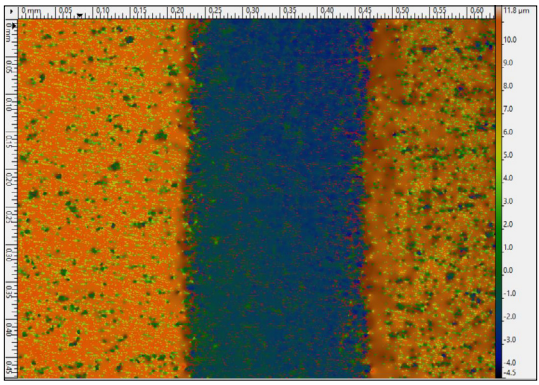

Figure 8. *A detail of the "ditch" formed by the needle during tribological examination.*

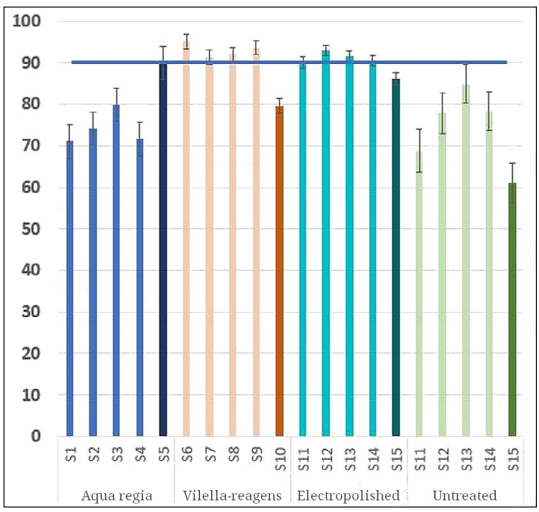

Figure 9. *Results of edge angle measurement. Samples S5, S10, S15 and S20 are uncoated reference pieces.*

4. Conclusions

Summarizing the above results, we found that etching solutions used in the literature can be used well for material type 316L and create a nice uneven surface, which affects the properties of the coating adhesion. Furthermore, we found that comparing the three different surface treatment methods to the surface of the Villela-treated inserts, the polymer adhered better than to the electropolished surface formed by the currently most widely used method. In this case, the coefficients of friction were also much lower than in the case of polished samples, so this surface treatment method may be suitable for strengthening the adhesion of the coating. Furthermore, using this surface treatment method based on the edge

angle values, i.e. the wettability conditions, we can say that we have obtained a better result than in the conventional electropolishing method.

Nevertheless, the surface treatment and coating processes have been automated and a suitable surface treatment method has been found for better coating adhesion on 316L inserts, however, further research and studies on stents are also needed.

Acknowledgements

Made with the support of the Ministry of Human Resources ÚNKP-18-3-II New National Excellence Program.

References

[1] Nazneen F., Herzog G., Arrigan D. W. M., Caplice N., Benvenuto P., Galvin P., Thompson M.: *Surface chemical and physical modification in stent technology for the treatment of coronary artery disease*. Journal of Biomedical Materials Research – Part B Applied Biomaterials 100B/7. (2012) 1989–2014. https://doi.org/10.1002/jbm.b.32772

[2] Sydow-Plum G., Tabrizian M.: *Review of stent coating strategies: clinical insights*. Materials Science and Technology, 24/9. (2008) 1127–1143. https://doi.org/10.1179/174328408X341816

[3] Mani G., Feldman M. D., Patel D., Agrawal C. M.: *Coronary stents: A materials perspective.* Biomaterials, 28/9. (2007) 1689–1710. https://doi.org/10.1016/j.biomaterials.2006.11.042

[4] Wienke H., Sawitowski T., Wnendt S., Fischer A., Dirsch O., Karoussos I. A., Erbel R.: *Stent Coating: A new approach in interventional cardiology*. Herz, 27/6. (2002) 518-526. https://doi.org/10.1007/s00059-002-2405-4

[5] De Scheerder I., Sohier J., Wang K., Verbeken E., Zhou X. R., Froyen L., van Humbeeck J., Piessens J., van de Werf F.: *Metallic Surface Treatment Using Electrochemical Polishing Decreases Thrombogenicity and Neointimal Hyperlesia of Coronary Stents*. Journal of Interventional Cardiology, 13/3. (2007) 179–185. https://doi.org/10.1111/j.1540-8183.2000.tb00286.x

[6] Lutter C., Nothhaft M., Rzany A., Garlichs C. D., Cicha I.: *Effect of specific surface microstructures on substrate endothelialisation and thrombogenicity: Importance for stent design.* Clinical Hemorheology and Microcirculation, 59/3. (2015) 219–233. https://doi.org/10.3233/CH-141839

[7] Horicsányi K., Asztalos L., Károly D., Fazakas É.: *Effect of Expansion Pressure ont he Drug Eluting Coating of Coronary Stents*. Acta Materialia Transylvanica, 1/1. (2018) 37–40. https://doi.org/10.2478/amt-2018-0012

[8] Sélley T. L., Terdik A. A., Bognár E.: *Biológailag lebomló polimerbevonatok tapadásának vizsgálata.* Fiatal Műszakiak Tudományos Ülésszaka, 18. (2013). 359–362. https://doi.org/10.36243/fmtu-2013.78

[9] Sojitra P., Engineer C., Raval A., Kothwala D. M.: *Surface enhancement and characterization of L-605 cobalt alloy cardiovascular stent by novel electrochemical treatment*. Trends in Biomaterials and Artificial Organs, 23/2. (2009) 55–64.

[10] Diaz-Rodriguez S., Chevallier P., Paternoster C., Montaño-Machado V., Noël C., Houssiaub L., Mantovani D.: *Surface modification and direct plasma amination of L605 CoCr alloys: on the optimization of the oxide layer for application in cardiovascular implants*. RSC Advances, 9/4. (2019) 2292–2301. https://doi.org/10.1039/C8RA08541B

[11] Gellér Zs. E., Albrecht K., Dobránszky J.: *Electropolishing of coronary stents*. Materials Science Forum, 589. (2008) 367–372. https://doi.org/10.4028/www.scientific.net/MSF.589.367

[12] Zhao H., Van Humbeeck J., Sohier J., De Scheerder I.: *Electrochemical polishing of 316L stainless steel slotted tube coronary stents*. Journal of Materials Science: Materials in Medicine, 13. (2002) 911–916. https://doi.org/10.1023/A:1019831808503

[13] Ozsváth P., Bognár E.: *Sztentbevonatok tapadásának vizsgálata és fejlesztése*. Anyagok Világa, 1/18. (2010) 1–9.

sciendo

Acta Materialia Transylvanica 3/2. (2020) 76–80.
DOI: hungarian: https://doi.org/10.33923/amt-2020-02-04
english: https://doi.org/10.33924/amt-2020-02-04

ACTA MATERIALIA TRANSYLVANICA

Investigation of the Effect of Process Parameters on the Break of Laser-welded Drill Bits

Attila Zsolt KENÉZ,[1,2] Gyula BAGYINSZKI[3]

[1] *Hilti Tools Ltd., Kecskemét, Hungary, attila.kenez@hilti.com*

[2] *Óbuda University, Doctoral School on Materials Sciences and Technologies, Budapest, Hungary, kenez.attila@phd.uni-obuda.hu*

[3] *Óbuda University, Donát Bánki Faculty of Mechanical and Safety Engineering, Budapest, Hungary, bagyinszki.gyula@bgk.uni-obuda.hu*

Abstract

The geometry and microstructure of the seam can be influenced by changing technological parameters such as laser power, welding speed, focus distance and shielding gas. In this research we examine the effect of laser power and focus distance on the quality of the breaking torque value while the welding speed and the shielding gas is unchanged. From the test results, we found that changing the defocus has no effect; a change in laser power affects ~15 %, while a change in welding position significantly affects the breaking torque.

Keywords: *laser welding, diamond segment, material testing, parameter study.*

1. Introduction

Laser beam welding has several advantages due to its concentrated nature: low heat input, a narrow heat affected zone, small distortion and easy automation. Compared to conventional welding processes, it produces deeper melting, higher welding speed, accuracy, reliability, efficiency and higher productivity [1]. Metal based materials of different material qualities can also be welded by laser beam if the two metals can simultaneously melt and form a common melt [2]. The weld geometry and micro-structure can be influenced by changing the technological parameters.

In our previous article [3] we have already investigated laser beam welded joints of diamond segment drill bits, searched for welding defects. Possible alloys and microstructure and hardness tests were performed. Additionally, in this research, we welded powder metallurgy segments onto thin-walled steel tubes, we used the same components for the sample production as for the serial production. The different effect of the laser welding process parameters was investigated separately onto the mixed joints fracture test values. This value is included in the current drawing specifications and is used to qualify laser-welded joints in serial production.

2. Conditions for the experiments

Laser welding process parameters, such as laser power, welding speed, focus distance and shielding gas have the greatest influence on the quality of welded joints [4]. In this series of experiments, besides the laser power, the effect of the change of the focus distance was investigated not only perpendicular direction to the surface (defocus) but also axial direction (welding position) (Figure 1), because when welding two components, the shift of the laser beam affects the joint strength.

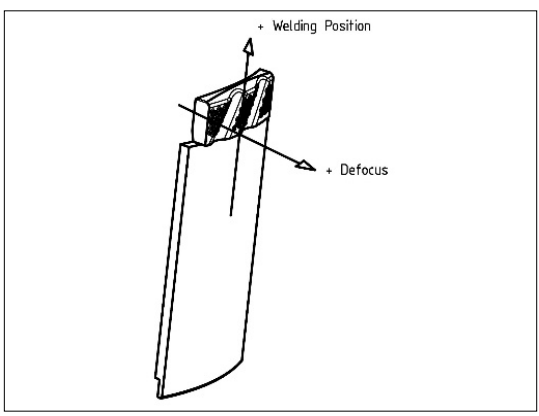

Figure 1. *Focus spot shifting directions*

The experiments were performed with a Trumpf TruDisk 4002 laser source, which has max. 4 kW power and beam wavelength of 1.03 μm. The segments were welded to a thin-walled cold drawn tube of material quality 1.0308 according to EN 10305-1 [5], with a wall thickness of 2±0,15 mm. The chemical composition of the segments: Astaloy-Mo powder = 99.8 %, Graphite powder = 0.2 %, and the chemical composition of the tube: C ≤ 0.17 %, Si ≤ 0.35 %, Mn ≤ 1.2 %, P ≤ 0.025 %, S ≤ 0.025 %.

Possible strategies for experiments:

- Best-guess approach is often used, but it is unsure that we can find the optimal solution. If we find a reasonably good solution, we need not keep guessing;
- Change one factor at a time is an easily reproducible procedure, but a large number of experimental steps are required, the interaction of the individual factors is not apparent from the experiment and interfering effects cannot be taken into account during the study;
- Factorial Experiments; changing several factors at the same time (fewer experimental steps required), the interaction of each factor is also apparent from the experiments. It is possible to calculate the average values and so-called effects associated with the settings.

To perform the experiments, we chose the change one factor at a time method. From the results obtained, we will be able to select the range within which it is worth conducting the factor experiments in order to understand the interaction of the parameters.

3. Results achieved

3.1. Test method used

The purpose of the test was to determine the average torque required to break out the segment, which should be greater than the required minimum 9 Nm. To determine the breaking torque value, we placed an insert that fitted the shape of the segment, which connected to digital display torque wrench (Figure 2). After setting the torque wrench at zero, the segment broke in an outward direction and the displayed value was read.

We broke 16 pcs of segments from each sample and evaluated the results with the Minitab software. An average breaking torque value applies to our specification ($\overline{X}$) but it is also important for us to have a lowest breaking torque value (min) to ensure that each bond meets the requirement. In addition, standard deviation (σ) and process capability (Cpk) were determined. The value of the latter shows how central to the mean and how far each value is relative to the tolerance. (Figure 3). The process capability index has two parts: upper process capability index (1) and lower process capability index (2). Cpk (3) is the smaller of the two [6]. In our case we just calculated with (1) because the tolerance in the classical term is a one-sided tolerance with a minimum requirement of 9,5 Nm.

If Cpk value is:

- > 1, the process is satisfactory, below which it does not meet the minimum requirements;
- ≥ 2, then the process is as expected, the number of defective pieces is approx. 5 PPM;
- ≥ 5, the process is redesigned (there is no need for such good quality or any additional cost involved).

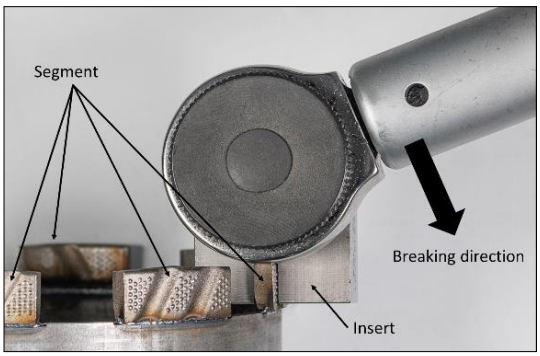

Figure 2. *Tools needed to determine the breaking torque value*

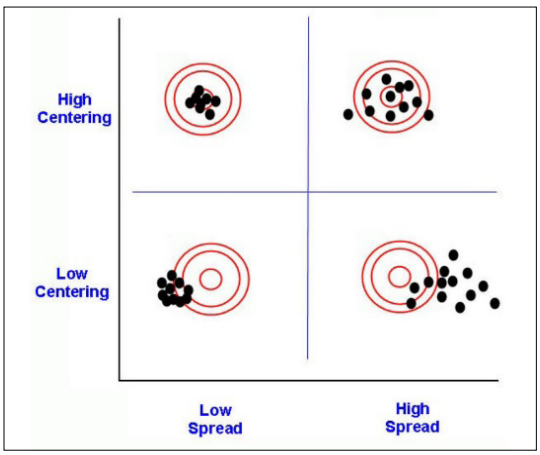

Figure 3. *Relationship between process spread and centrality (Symbols in the figure: black dots show the measured values; the red circles show the tolerance fields and the intervention limit)* [7]

$$C_{PL} = \frac{Mean\ value - Lower\ tolerance}{3 \times Deviation} \quad (1)$$

$$C_{PU} = \frac{Upper\ tolerance - Mean\ value}{3 \times Deviation} \quad (2)$$

$$C_{PK} = Min(C_{PL}, C_{PU}) \quad (3)$$

The initial value was set to 0.25 mm defocus and (−0.2) mm welding position, the welding speed was set to the maximum value that could be set on the laser welding device, 3 m/min during the experiments.

3.2. Results and their evaluation

The laser power was reduced in increments of 10% until the tube had just melted completely, this was achieved in Sample Nr. 5 (at 45% laser power). The data is shown in **Table 1** and the graphical representation is shown in **Figure 4.** The breaking torque values were varied in between 2 Nm in the power range of 45–70 %. The lowest standard deviation, the highest machine index and highest breaking torque index occurred at 60 % power. However, 45 % laser power for the melting criterion was considered for further experiments since this parameter is immediately visible if the tube does not melt through on the entire cross-section due to focus spot offset.

The defocus was varied in increments of 1mm starting from the surface (positive direction) and then, in 0.5 mm increments was moved below the outer surface of the tube (negative direction). The data is shown in **Table 2.** and the graphical representation is shown in **Figure 5.** The positive defocus has a negative effect on the breaking torque index, but as a result of the negative defocus provides changes on the breaking torque values within 1.4 Nm range. For the analysis of the welding position, the parameter with the highest machine capability index was chosen (Sample No. 7).

The welding position was varied in increments of 0.1 mm from the segment edge in the direction of the tube. The data is shown in **Table 3.** and the graphical representation is shown in **Figure 6.** The welding position away from the edge of the segment increases the breaking torque value, and when the maximum is reached, the standard deviation increases, and in parallel, the breaking

Table 1. *Change of breaking torque values as a function of laser power*

Sample sign	$\overline{X}$ (Nm)	σ	Cpk	min (Nm)
1 (70 %)	17.575	1.640	2.65	12.1
2 (60 %)	19.506	0.589	3.68	17.4
3 (50 %)	18.793	2.216	1.78	11.1
4 (40 %)	14.773	0.611	2.84	13.7
5 (45 %)	17.620	1.108	2.56	14.3

Table 2. *Change of breaking torque values as a function of defocus*

Sample sign	$\overline{X}$ (Nm)	σ	Cpk	min (Nm)
6 (1.25)	13.431	1.271	1.58	10.1
7 (−0.75)	17.731	0.690	4.69	16
8 (−1.25)	17.818	1.104	2.74	15.5
9 (−1.75)	17.275	1.025	2.39	15.6
10 (−2.25)	17.086	1.823	1.73	11.7
11 (−2.75)	16.433	1.848	1.35	10.9

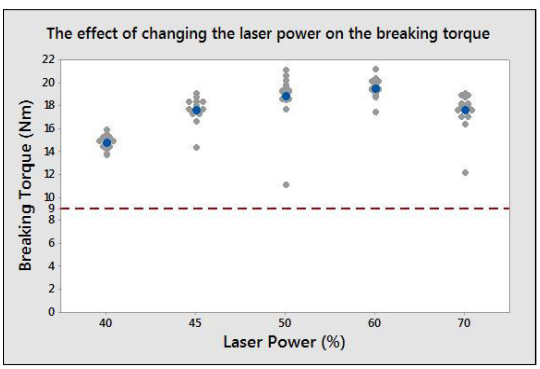

Figure 4. *Change of breaking torque values as a function of laser power*

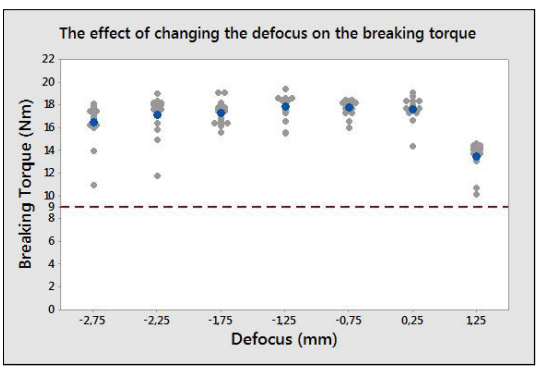

Figure 5. *Change of breaking torque values as a function of defocus*

Table 3. *Change of breaking torque values as a function of welding position*

Sample sign	$\overline{X}$ (Nm)	σ	Cpk	min (Nm)
13 (0)	13.025	1.105	2.05	11.2
14 (−0.1)	15.500	1.044	2.59	14.2
15 (−0.3)	14.450	2.134	0.89	10.4
16 (−0.4)	3.612	5.106	−0.39	0
17 (−0.5)	0			0

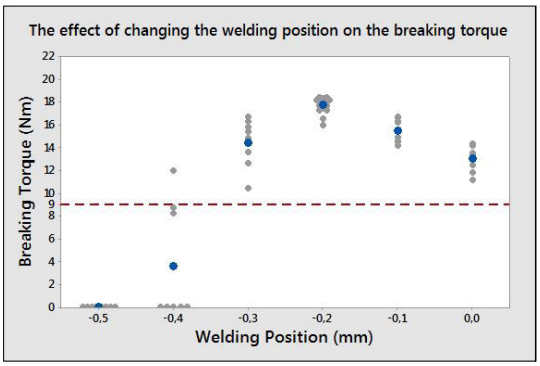

Figure 6. *Change of breaking torque values as a function of welding position*

torque value drops below the required minimum of 9 Nm (Sample No. 16 and 17).

Following the one factor change at a time strategy, we came to a good solution with parameters: 45 % laser power, −0.75 mm defocus, −0.2 mm welding position.

4. Conclusions

Focus spot offsets only show proper results at 45% of laser power, other offsets gave the highest machine capability index when different laser power was used. To verify this point, we performed an experiment using the above offsets at 60 % laser power, resulting Cpk of 0.77 (as opposed to 4.69).

The disadvantage of this strategy is that we do not know the interactions of the factors, but from the results we have selected the ranges within which the factor experiments are worth performing: 45–70 % laser power, defocus 0.75–(−1.25) mm, welding position 0.00–(−0.3) mm. We also want to know the effect of speed, so we have included it in the range of 30-50 mm/s.

The breaking torque charts show more than just the change of the values. It also can be observed from the laser power diagram that the average breaking torque index of Sample No. 1 and Sample No. 5 differs only by 0.1 Nm and there is also a difference of 0.1 in the machine capability index. From this it can be concluded that the two seams have same load capacity, but this can be determined by further detailed investigations, since there was a significant difference in the laser power, i.e. due to different heat input, the weld width, hardness value and microstructure should be examined in addition.

The optimum laser power can be determined at 60 %, as it has the highest average breaking torque value, lowest standard deviation, highest Cpk value, but the load capacity of joint does not deteriorate as the power changes. This is also shown in **Figure 5.** the defocus does not affect the breaking torque value within the tube wall thickness (0–(−2) mm). The welding position has the greatest effect on the breaking torque value, the change of this parameter sharply deteriorates the joint quality if the change is greater than ±0.1 mm.

We can also observe the so-called „Outliers" in **Figures 4.** and **5.** These values are farther from the mean value, but above the specified value (e.g., Sample No. 10, segment Nr. 3 had a 11.7 Nm, segment Nr. 4 had a 17.3 Nm). Visual inspection of the seams after welding did not show any surface damage, leakage to the surface, welding defects. More detailed microscopic examination (e.g. optical light microscopy or scanning electron microscopy) could determine the difference between the seams.

References

[1] M. Li, Z. Li, Y. Zhao, H. Li, Y. Wang, J Huang: *Influence of Welding Parameters on Weld Formation and Microstructure of Dual-Laser Beams Welded T-Joint of Aluminum Alloy.* Advances in Materials Science and Engineering, 2011. https://doi.org/10.1155/2011/767260

[2] Bagyinszki Gy., Bitay E.: *Nagy energiasűrűségű eljárások hegeszthetőségi szempontjai.* In: Fiatal műszakiak tudományos ülésszaka XVII., Műszaki Tudományos Füzetek, 2012. 13–18. https://doi.org/10.36243/fmtu-2012.006

[3] Kenéz A. Zs., Bagyinszki Gy.: *Gyémánt fűrószegmensek lézeres hegesztésének vizsgálata.* Acta Materialia Transylvanica, 1/2. (2018) 85–88. https://doi.org/10.2478/amt-2018-0030

[4] M. P. Prabakaran, G. R. Kannan: *Optimization of CO_2 Laser Beam Welding Process Parameters to Attain Maximum Weld Strength in Dissimilar Metals.* Materials Today: Proceedings, 5. (2018) 6607–6616. https://doi.org/10.1016/j.matpr.2017.11.316

[5] EN 10305-1: Steel tubes for precision applications – Technical delivery conditions. Part 1: Seamless cold drawn tubes, 2002.
[6] Hessing T.: *Process Capability (Cp & Cpk).* On 6sstudyguide.com https://sixsigmastudyguide.com/process-capability-cp-cpk/
[7] Hessing T.: *Process Capability & Performance (Pp, Ppk, Cp, Cpk).* On 6sstudyguide.com https://sixsigmastudyguide.com/process-capability-pp-ppk-cp-cpk/

sciendo

Acta Materialia Transylvanica 3/2. (2020) 81–85.
DOI: hungarian: https://doi.org/10.33923/amt-2020-02-05
english: https://doi.org/10.33924/amt-2020-02-05

ACTA MATERIALIA TRANSYLVANICA

Microstructural Changes During Laser Beam Welding of Austenitic Stainless Steel Sheets

Ferenc KOVÁCS,[1] Enikő Réka FÁBIÁN[2]

Óbuda University, Bánki Dónát Faculty of Mechanical and Safety Engineering, Institute of Materials and Manufacturing Sciences. Budapest, Hungary

[1] *kovacsferi1996@gmail.com*

[2] *fabian.reka@bgk.uni-obuda.hu*

Abstract

The purpose of our study was to investigate the properties of welded joints formed by 1.5 mm thick plates with a diode laser beam equipment. The technological parameters influence the shape of the weld metal. In the heat affected zone no grain coarsening appeared. Increasing the welding speed, in case of similar laser power, the ferrite content of weld metal decreases. The hardness' of the streams are higher than that of base metal, but the highest values were measured in heat affected zones.

Keywords*: diode laser, austenitic stainless steel, welding, ferrite content.*

1. Introduction

One of the new technologies to be exploited in the 21st century is the increasingly available laser welding. Due to the velocity of the concentrated beam and its repetitive accuracy it stands out from other technologies [1–3]. Laser beam welding plays an increasingly important role in welded structures today due to the concentrated heat input and the high welding speed. Laser beam welding works with concentrated heat input, making it suitable for welding of high alloyed austenitic steels. Generally, the heat-affected zone is small, no grain coarsening is created, consequently the structure will have good mechanical properties and the corrosion properties will be favorable as well. In return for its advantages, laser welding requires accurate preparation before welding [1–5].

The properties of laser welding machines are extremely diverse compared to laser radiation sources. The radiation source determines the wavelength of the laser beam, which affects the absorption. For instance, the CO_2 laser with a wavelength of 10.6 µm is expected to have a low interaction time and deep beet-shaped melting, called keyhole welding. The other mode is heat conduction welding, where the energy of the laser beam reaches to deeper layers of the product from the surface by heat-conduction. This behavior is produced, for example, by the diode laser in this study with its 0.94 µm wavelength, which is called half-lens-shaped in the scientific literature.

The sources of the laser beam in the case of keyhole welding are the carbon dioxide laser and the Nd: YAG lasers. The welding speed is less than 12 m/min and the weldable plate thickness is less than 25 mm. Laser beam intensity is higher than 10^6 W/cm^2 in the case of steel welding. With this method can be welded unalloyed and high-alloyed steels, aluminium and its alloys, copper and its alloys, pairs of materials of different metals [4].

Typical radiation sources for the heat-conduction process are Nd: YAG lasers, fiber laser and diode laser. The intensity of the laser beam in the case of steels is less than 10^6 W/cm^2 [6]. According to the literature, this process is suitable for welding high-alloy steels as well. The weldable plate thickness without any filler material with a diode laser beam can be increased with laser beam power [6]. The laser beam processes are influenced by the focus point position as well as by the focus path parameters [7–9]. A common feature of laser beam methods is that the heat input and the heat transfer are influenced by the absorption

and geometric conditions. As reported in the literature [10], the absorption of a laser beam in the case of a CO_2 laser is about 10 %, whereas with application of a diode laser it increases to 30 %. The roughness of the surface also influences significantly the absorption coefficient of the laser beam. The absorption coefficient varies between 4–80 % in the case of CO_2 laser beam treatments, but in case of the solid-state laser beam treatments it can reach 30 % even on polished surfaces [11]. The basic principle of a diode laser is same as all the other laser's, with an additional characteristic that the formation of the population inversion requires a particularly high current density, thus it is advisable to use the material, which is to be excited, with a minimum volume. It is advisable to organize several units into modules for the required performance. This is one of the favourable characteristics of the diode laser: the small laser beam source can be placed at the end of the robotic arm. Obviously, there is no consuming laser gas, and these two effects can result in significant cost savings and space requirements. Yet, the diode laser is rare in welding applications because of the energy density mentioned above.

2. Material and Testing

The 1.4404 austenitic corrosion-resistant steel selected for the experiment can be easily cold formed and is a weldable quality steel. This steel is also often used in the construction of chemical and textile structures because of its high resistance to aggressive media, its resistance to inter-crystalline corrosion up to 400 °C, and its low cost compared to other austenitic grades [12]. The purpose of our study was to investigate the properties of welded joints made of 1.5 mm thick plates with diode laser beam equipment. In case of LDL 130-3000 laser beam apparatus used, the energy distribution of the radiation source is very abundant, the focus is oval, 3 mm long and 1 mm transverse. The weld metal was protected by argon gas at a yield of 15 L/min on the crown side and 10 L/min on the root side. The nozzle was at an angle of 30° to the workpiece. During to laser beam welding, the temperature of the weld bath could be monitored on a monitor, which was always between 1400 °C and 1500 °C. When the laser beam stopped, the temperature of the seam decreased at high speed and the piece became quickly touchable.

For metallographic examination, 10×30 mm samples were cut at 25 mm from the streams end. 2-2 specimens with 15×30 mm dimensions were prepared for corrosion testing from the central region of the seam. The ferrite content was measured by Fischer FMP30. Ferritescope using a magnetic induction type. The ferrite content of the welds at crown and root portion of the stream weld, and also the weld metal on metallographic prepared samples were measured. Our metallographic studies tested several etching materials. The γ and δ phases can be distinguished after etching with Kalling'2 reagent, but the austenitic structure of the base material became more visible after aqua regal etching. Microstructure of welded zone were studied on Neophot-2 type microscope.

Microhardness measurement was carried out with a load of 0.2 kg. Corrosion tests were performed according to ASTM G48 standard method B in 6 % $FeCl_3$ aqueous solution.

3.Results

We could create properly fusible seams with a 1000-1200 W power and a welding speed between 4–8 mm/s. Applying 1000 W the welding speed had to be 4–6 mm/s. Increasing the laser power from 1000 W to 1200 W when the welding speed was 6 mm/s the ratio of height to width decreased from H/D= 5/3 to 1/2 as can be seen in **Figure 1.**

The heat-affected zone of the seams is extremely narrow, almost indistinguishable by aqua regal etching, but etching with Kalling's reagent separates a narrow ferritic band at the edge of weld metal, which is narrower than the midline ferritic enrichment in the middle of the parent material plates, as shown in **Figure 2.** There was no grain coarsening in heat affected zone.

Consistent with the microscopic observations, the percentage of ferrite on the surface of the plates, measured with a ferrite microscope, was 0.01 % on average, while in the center line 0.3 %. After welding, the ferrite content of the weld metal increased. The ferrite content of the weld metal with the highest heat input exceeded 5 % when the measurements were executed on the crown part, but almost reached 4 % measured on the metallographically prepared samples (**Figure 3**).

The microhardness measurement data show a good agreement with the results measured with a ferrite scope. Samples with higher ferrite content have higher average hardness. The highest hardness was measured in the heat-affected zones, but nowhere exceeded 200 HV0.2. Welding with same laser power the highest hardness was measured at the lowest welding speed. (**Figure 4**).

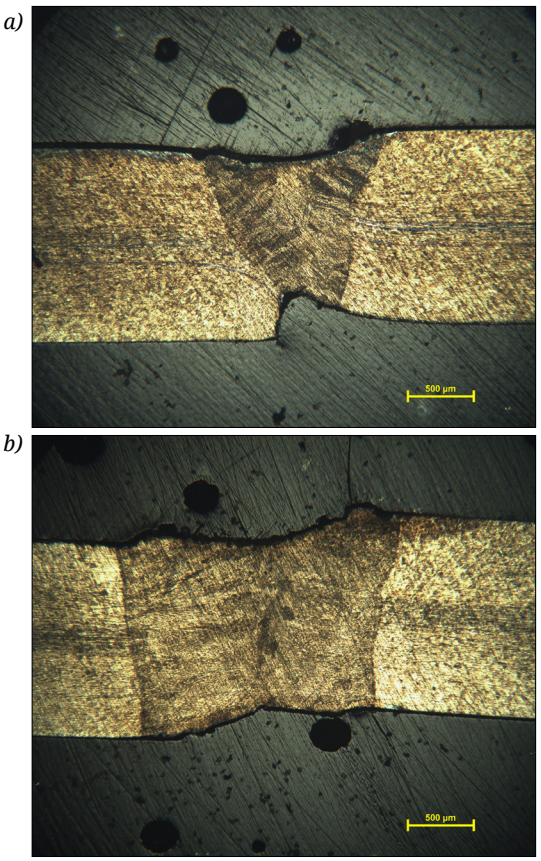

Figure 1. *Laser welding power effect on geometry of welding streams. v = 6 mm/s Kalling reagent a) P = 1000 W, b) P = 1200 W.*

Testing the resistance of the weld areas to pitting corrosion in a 6 % aqueous solution of $FeCl_3$ by soaking method showed little pitting corrosion after 24 hours, but after 72 hours several holes were observed in the vicinity of the joints, especially in samples with wider widths, as shown in **Figure 5**.

4. Conclusions

Austenitic stainless-steel sheets, with 1.5 mm thickness, were welded by diode laser welding equipment, at 1000–1200 W. Despite the fact that no filler material was used, the ferrite content of the weld metal in the crown part exceeded 3 %, this was slightly lower in the sections. At the same plate thickness, using the same welding power, it can be shown that the ferrite content of the weld metals, measured with a ferritescope, decreases with increasing welding speed. It can be seen that the hardness of the seams increases compared to

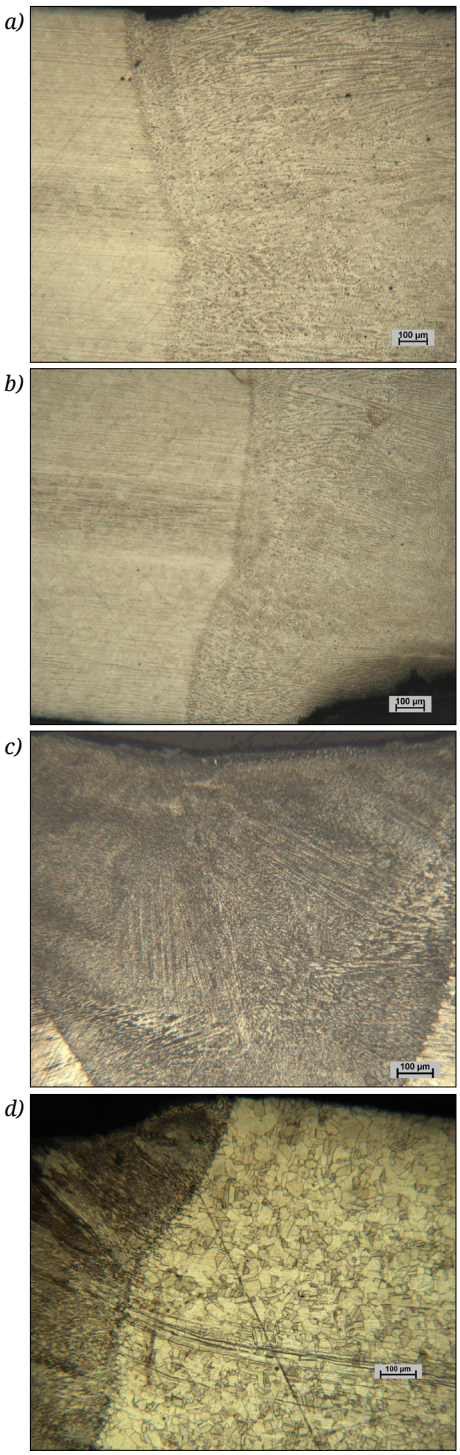

Figure 2. *Micrographs on weld metals zone a) 1200 W, 4 mm/s. Kalling reagent, b) 1200 W, 6 mm/s. Kalling reagent, c) 1200 W, 8 mm/s. Kalling reagent, d) 1000 W, 6 mm/s. aqua regal.*

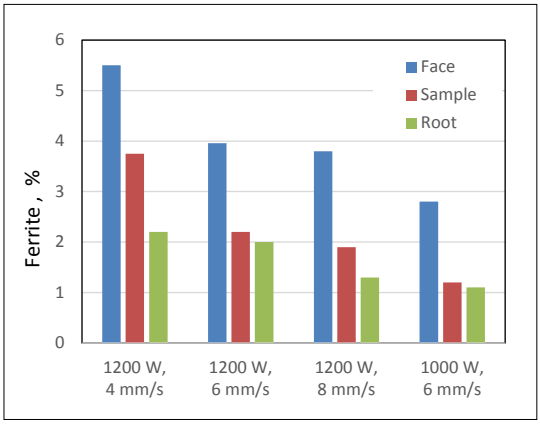

Figure 3. *Laser welding parameters effect on ferrite content of the weld metals.*

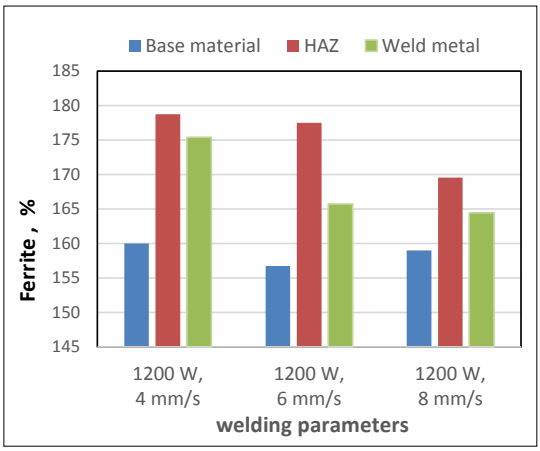

Figure 4. *Laser welding parameters effect on hardness after welding.*

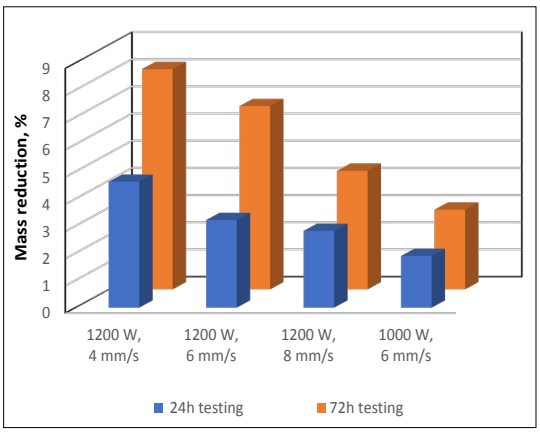

Figure 5. *Laser welding parameters effect on pitting corrosion.*

the base material at each welding speed, but the highest hardness was measured in the heat-affected zones, which can be related to the amount of delta ferrite.

Acknowledgement

The work would not have been created without the help of Budai Benefit Ltd.

The authors acknowledge the financial support of this work by the Hungarian State and the European Union under the EFOP-3.6.1-16-2016-00010 project.

References

[1] Bagyinszki Gy., Bitay E.: *Hegesztéstechnika I. Eljárások és gépesítés*. Műszaki Tudományos Füzetek 9., EME, Kolozsvár, 2010. https://doi.org/10.36242/mtf-09

[2] Bagyinszki Gy., Bitay E.: *Hegesztéstechnika II. Berendezések és mérések*. Műszaki Tudományos Füzetek 10., EME, Kolozsvár, 2010. https://doi.org/10.36242/mtf-10

[3] Kreisz I.: *Lézersugárforrások*. Edutus Főiskola, 2012. 45–57.

[4] Buza G.: *Lézersugaras technológiák 1*. Edutus Főiskola, 2012. 75.

[5] Bitay E., Bagyinszki Gy.: *Nagy energiasűrűségű hegesztési eljárások több szempontú rendszerezése / Multi respect classification of high energy density welding process*. XV. FMTÜ, EME, Kolozsvár, Románia, 2010. 55–65. https://doi.org/10.36243/fmtu-2010.13

[6] Alcocka A., Baufeld B.: *Diode laser welding of stainless steel 304L*. Journal of Materials Processing Technology, 240. (2017) 138–144.

[7] Meszlényi Gy., Bitay E.: *A fókuszált lézernyaláb keresztmetszeti jellemzőinek szerepe az impulzusos üzemű lézeres vágásnál / Role of the Features of Focused Laser Beam at Pulsed Laser Cutting*. Acta, Materiala Transylvanica, 2/2. (2019) 115–120. https://doi.org/10.33924/amt-2019-02-09

[8] Meszlényi Gy., Bitay E.: *A fókuszhelyzet szerepe erősen reflektáló anyag egyimpulzusos, lézersugaras fúrásakor / The Role of Focus Position in Single Pulse Laser Drilling of Highly Reflecting Materials*. Acta Materiala Transylvanica, 2/1. (2019) 61–68. https://doi.org/10.33924/amt-2019-01-10

[9] Meszlényi Gy., Bitay E.: *Az egyimpulzusos lézersugaras fúrás folyamatának elemzése*. Bányászati és Kohászati Lapok – Kohászat, 151/5–6. (2018) 40–44. https://www.ombkenet.hu/images/2018/koh/Kohaszat_2018_5_6szam.pdf

[10] Laser Focus World Lasers&Surces (accessed on: 2020. feb. 24.) https://www.laserfocusworld.com/articles/2011/04/laser-marking-how-to-choose-the-best-laser-for-your-marking-application.html

[11] Lyubomir L., Angelov N.: *Physical model about laserimpacton metals and alloys*. Contemporary Materials, I/2. (2010) 124–128;
[12] Direct Line: *Rozsdamentes acélok jellemzői katalógus* (accessed on: 2020. feb. 15.) http://www.dldh.hu/wp-content/uploads/2012/02/Direct_Line_rozsdamentes_acelok_jellemzoi_katalogus.pdf

sciendo

Acta Materialia Transylvanica 3/2. (2020) 86–89.
DOI: hungarian: https://doi.org/10.33923/amt-2020-02-06
english: https://doi.org/10.33924/amt-2020-02-06

ACTA MATERIALIA TRANSYLVANICA

Experiments with Femtosecond Laser on Monocrystalline Silicon

Anna MALOVECZKY,[1] Márk WINDISCH,[2] Dávid SZABÓ,[3] Gábor BUZA,[4] Dávid UGI,[5] Miklós VERES,[6] István RIGÓ,[7] Péter FÜRJES,[8] Orsolya HAKKEL[9]

[1, 2, 3, 4] *Bay Zoltán Nonprofit Ltd. for Applied Research. Budapest, Hungary, anna.maloveczky@bayzoltan.hu, mark.windisch@bayzoltan.hu, david.szabo2@bayzoltan.hu, gabor.buza@bayzoltan.hu*

[5] *Eötvös Loránd University. Budapest, Hungary, ugidavid42@gmail.com*

[6, 7] *Wigner Research Centre for Physics. Budapest, Hungary, veres.miklos@wigner.mta.hu, rigo.istvan@wigner.mta.hu*

[8, 9] *Centre for Energy Research. Budapest, Hungary, furjes@mfa.kfki.hu, hakkel@energia.mta.hu*

Abstract

Experiments were performed with femtosecond laser on monocrystalline silicon for different application fields. The small focal spot diameter, the ultra-short pulse length, and the high energy density opens new ways in material processing; the treated material will have smaller heat affected zone (HAZ), and allow more precise, higher quality material processing. Micropillars and LIPSS structures were prepared on monocrystalline silicon in our study.

Keywords*: femtosecond laser, surface structuring, micromachining, micropillar.*

1. Introduction

Ultra-short pulsed lasers (i.e., pico- and femtosecond lasers) have undergone rapid development over the past few decades. These lasers have many advantages over conventional (e.g., nanosecond) pulsed lasers. As a result of extremely short pulses, the heat affected zone (HAZ) is much smaller in the treated materials, thus providing high quality micromachining for both ductile and brittle materials. This is because electrons need 1 to 100 ps - depending on the electron-phonon coupling strength of the material being treated - to transfer thermal energy to the nucleus in the lattice. In femtosecond lasers, this results in only a very small fraction of the irradiated energy being transformed into heat.

Another advantage of ultra-short pulsed lasers is that they are capable of generating extremely high peak pulse power, which allows the multi-photon absorption to take place, so that insulating materials (e.g. glass) can be machined with it. Single-photon absorption cannot excite the electrons of the insulating materials into the conduction band. However, due to the high photon density in multi-photon absorption, it is possible to excite the electrons into the conduction band even if the energy of the band gap is greater than that of the photon [1–6].

Because of these characteristics, femtosecond lasers are capable of ablation in high quality. Ablation: during high-power pulsed laser treatment, a plasma cloud of matter exits the material and leaves a well-defined cavity. This process is also called hyper sublimation: the solid enters directly to the plasma phase [1].

Micropillars, microchannels and stents can be machined this way.

Micropillars are used for material research purposes. Plastic deformation works differently at the micro level, and understanding it is important for designing micro-sized parts and developing dislocation theory. In the course of our work, pre-processed micropillars were machined to reduce the time-consuming work with FIB (Focused Ion Beam) [7–11].

Below the ablation threshold, regular, wave-like structures are known as Laser Induced Period-

ic Surface Structures (LIPSS) appear on the surface. The period of these waves is much smaller than the spot diameter of the laser beam. There is no accepted theory for the mechanism of their formation, but probably the interference of incident and backscattered electromagnetic waves and also hydrodynamic phenomena play a role in the formation of these structures. Such structured surfaces can be used, for example, to improve tribological properties, to form antibacterial surfaces, and as a substrate for SERS (Surface Enhanced Raman Scattering) spectroscopy. It is a common problem in Raman spectroscopy that the test component is only present in small amounts in the solution, such as in spinal fluid testing or in detecting drug molecules remaining in filtered water. In this case, the Raman sign of the material is not large enough to detect its presence. A SERS chip (substrate) is then inserted into the Raman microscope. By dropping the test solution to this substrate the Raman signal of the test component can be enhanced up to 1014 fold [12, 13].

The main (electromagnetic) reason for SERS enhancement is: The external electromagnetic field causes the free electrons on the surface of the metals to oscillate: this is a quasi-particle called plasmon. If they have a resonance frequency equal to that of the outer field, then the intensity of the electromagnetic field is amplified. This can mean amplifying the electromagnetic fields of the exciter or the scattered one, or even both[14, 15].

Of course, not only laser beam technology can be used to produce the structures for the uses detailed above, for example, the preparation of a SERS substrate can also be achieved by electrochemical methods. However, laser beam treatments have many advantages: high productivity, repeatability, precision machining and localization [1].

1.1. Laser and investigating devices

The laser source is a Coherent Monaco type resonator. Laser radiation is transmitted without fibres, through mirrors to the z-compensation lens (from Scanlab), then to the galvanic mirrors of the F-theta lens. The repetition rate is adjustable from 188 kHz to 50 MHz, which also allows the equipment to be used in industrial applications. The pulse length is adjustable from 300 fs to 10 ps. The average maximum power is 62 W and the maximum pulse energy is 200 µJ. However, the maximum peak pulse power is 600 MW, which means extremely high energy density. By comparison, the approximate performance of 1 Paks Nuclear Power Plant units is 500 MW. The laser wavelength is 1064 nm and the focal spot diameter is 80 µm.

Images were taken by with a Keyence VHX 2000 microscope a FEI Quanta FEG 3D scanning electron microscope.

Raman spectroscopic investigations were carried out with a Renishaw InVia micro-Raman spectrometer.

1.2 Micropillars

It can take up to a day to prepare one micropillar with FIB. During our work we developed pre-processed micro columns with a femtosecond laser, which was later refined with FIB post-process. With our laser equipment, hundreds of pre-processed micropillars can be made in minutes.

During the preparation of the micro-columns, trenches were made in grid arrangement into monocrystalline silicon. Thus micropillars were formed between the trenches. Pillars with a height of a few tens of micrometres up to a millimetre were formed (see Figures 1, 2).

For the material physics model it is important that the pillar should remain a perfect single crystal. So the presence of a heat affected zone is not allowed. For smaller, 20–60 micrometre high pillars, negligible HAZ were measured with EBSD (Electron Backscatter Diffraction), which can be removed easily and quickly during the FIB post-processing. Larger, hundreds of micrometre-tall pillars have significant, 20–30 micrometres thick HAZ. However, the HAZ can be further reduced in this case by optimizing the parameters of the laser beam treatment: laser power, time between scan repeat, use of refrigerant.

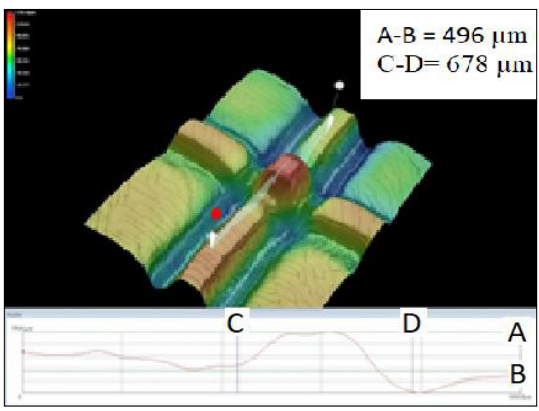

Figure 1. *3D optical microscope image of a 500 micrometre high micropillar and its topographic graph.*

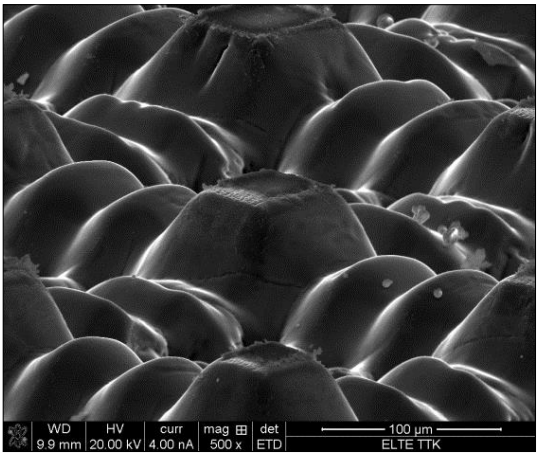

Figure 2. *SEM image of a 50 micrometre high micropillar.*

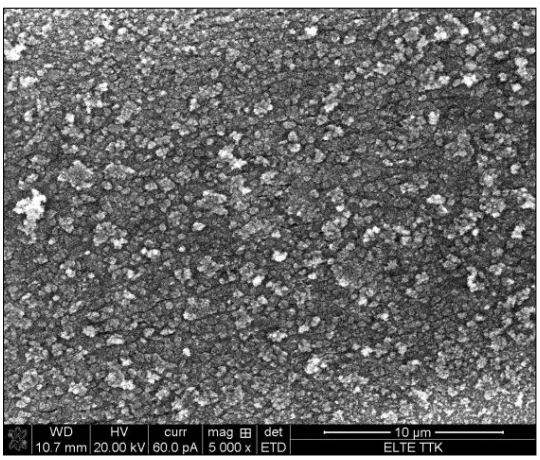

Figure 4. *SEM image of the sample with 360X enhancement factor, without gold coating*

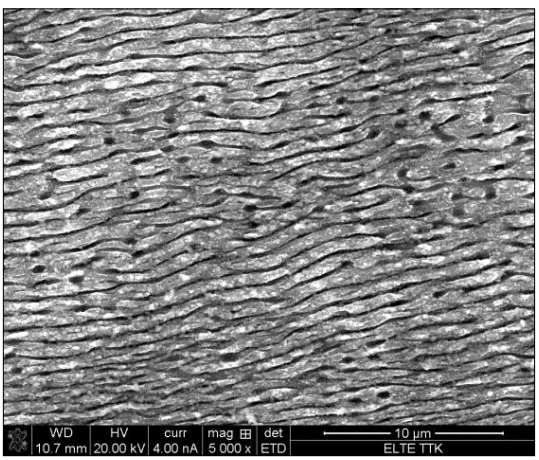

Figure 3. *SEM image of the sample with 360X enhancement factor, without gold coating.*

1.3. LIPSS

If the energy density is close to, but is below the ablation threshold, LIPSS will develop along the scanned lines. The period of the LIPSS is approximately equal to the incident laser's wavelength. The depth and morphology of the LIPSS (and thus its amplification factor) depends on the laser beam parameters used, so in this paper only two representative samples will be introduced (see **Figures 3–4**).

A 150 nm thick gold layer was evaporated onto the LIPSS-structured monocrystalline silicon surface and the enhancement factor was determined using a Raman spectrometer. A sample of benzophenone solution was dropped to the substrate, and the reference signal was measured on a silicon surface with 150 nm gold, but without LIPSS. The enhancement factor was 360X in one case and 490X on the other sample. The exciting laser used in the Raman spectrometer had a wavelength of 610 nm and an exposure time of 1 second.

The two samples differed in their scanning speed: with the scanning speed one magnitude lower, the enhancement factor was higher. Increasing the enhancement factor is favoured by a homogeneous structure composed of several small particles, which can be achieved by slower scanning.

2. Conclusion

In the course of our work we have created different surfaces on a monocrystalline silicon with a femtosecond laser.

Femtosecond laser machining of the pre-processed micropillars significantly reduced machining time with FIB, but further optimization of the laser parameters is desirable to reduce the HAZ.

LIPSS made by us with 150 nm gold coating greatly enhances the Raman signal of benzophenone. We plan to increase the enhancement factor further and to perform measurements with other sample molecules and excitation wavelengths.

We also plan to investigate the tribological performance of the surfaces with LIPSS.

References

[1] Mangirdas M., Albertas Ž., Satoshi H., Yoshio H., Vygantas M., Ričardas B., Saulius J.: *Ultrafast laser processing of materials: from science to industry.* Light: Science & Applications, 5. (2016) 16–133.

[2] Mathis A., Courvoisiera F., Froehly L., Furfaro L., Jacquot M., Lacourt P. A., Dudley J. M.: *Micromachining along a curve. Femtosecond laser mi-*

cromachining of curved profiles in diamond and silicon using accelerating beams. Applied Physics Letters, 101. (2012) 71–110. https://doi.org/10.1063/1.4745925

[3] Evgeny L.: *Mechanisms of femtosecond LIPSS formation induced by periodic surface temperature modulation.* Applied Surface Science, 374. (2016) 30.

[4] Kaiwen D., Cong W., Yu Z., Zheng X., Zhi L., Shu M., Biwei W.: *One-step fabrication of multifunctional fusiform hierarchical micro/nanostructures on copper by femtosecond laser*. Surface and Coatings Technology, 367. (2019) 244–251. https://doi.org/10.1016/j.surfcoat.2019.04.005

[5] Rafael R. G., Eric M.: *Femtosecond laser micromachining in transparent materials*. Nature Photonics, 2. (2008) 219–225.

[6] Andrius M., Saulius J., Mitsuru W., Masafumi M., Shigeki M., Hiroaki M., Junji N.: *Femtosecond laser-assisted three-dimensional microfabrication in silica*. Optics Letters, 26/5. (2001) 277–279. https://doi.org/10.1364/OL.26.000277

[7] Akarapu S., Zbib H. M., Bahr D. F.: *Analysis of heterogeneous deformation and dislocation dynamics in single crystal micropillars under compression.* International Journal of Plasticity, 26/2. (2010) 239–257. https://doi.org/10.1016/j.ijplas.2009.06.005

[8] Aifantis E. C.: *Gradient Deformation Models at Nano, Micro, and Macro Scales*. Journal of Engineering Materials and Technology, 121/2. (1999) 189–202.

[9] Eduardo B.: *Interpretation of the size effects in micropillar compression by a strain gradient crystal plasticity theory*. International Journal of Plasticity, 116. (2019) 31. https://doi.org/10.1016/j.ijplas.2019.01.011

[10] Tanga H., Schwarzb K. W., Espinosaa H. D.: *Dislocation escape-related size effects in single-crystal micropillars under uniaxial compression*. Acta Materialia, 55/5. (2007) 1607–1616. https://doi.org/10.1016/j.actamat.2006.10.021

[11] William D., Nix Seok W. L.: *Micro-pillar plasticity controlled by dislocation nucleation at surfaces.* Philosophical Magazine, 91/7–9. (2011) 1084–1096. https://doi.org/10.1080/14786435.2010.502141

[12] Jijo E. G., Unnikrishnan V. K., Deepak M., Santhosh C., Sajan D. G.: *Flexible Superhydrophobic SERS Substrates Fabricated by In Situ Reduction of Ag on Femtosecond Laser-Written Hierarchical Surfaces*. Sensors and Actuators B, 272/1. (2018) 485–493. https://doi.org/10.1016/j.snb.2018.05.155

[13] Steven E. J. B., Narayana M. S. S.: *Surface-Enhanced Raman Spectroscopy (SERS) for Sub-Micromolar Detection of DNA/RNA Mononucleotides*. Journal of the American Chemical Society, 128/49. (2006) 15580–15581. https://doi.org/10.1021/ja066263w

[14] Ximei Q., Jun L., Shuming N.: S*timuli-Responsive SERS Nanoparticles. Conformational Control of Plasmonic Coupling and Surface Raman Enhancement.* Journal of the American Chemical Society, 131/22. (2009) 7540–7541. https://doi.org/10.1021/ja902226z

[15] Zhu Z., Yan Z., Zhan P., Wang Z.: *Large-area surface-enhanced Raman scattering-active substrates fabricated by femtosecond laser ablation*. Science China Physics, Mechanics and Astronomy, 56. (2013) 1806–1809.

sciendo

Acta Materialia Transylvanica 3/2. (2020) 90–93.
DOI: hungarian: https://doi.org/10.33923/amt-2020-02-07
english: https://doi.org/10.33924/amt-2020-02-07

ACTA MATERIALIA TRANSYLVANICA

Investigation of Composite Behaviour of Lath Martensite

János Endre MARÓTI,[1] Péter János SZABÓ[2]

Budapest University of Technology and Economics, Faculty of Mechanical Engineering, Department of Materials Science and Engineering, Budapest, Hungary

[1] *maroti@eik.bme.hu*

[2] *szpj@eik.bme.hu*

Abstract

It is very important for our research that we are able to examine the orientation of packets and their relationship to directions of stress that cause plastic deformation. We use electron backscatter diffraction (EBSD) to achieve this. EBSD examination requires very careful sample preparation. In our work we have developed a sample preparation method for electron bakcscatter diffraction examination. In this study we present the method, which consists of multistage mechanical grinding, polishing and ion polishing. Optimal parameters for each steps (eg.: grinding, polishing and sputtering time, milling angle) were determined for lath martensitic steel, however, it could be used for other type of steel with minor adjustments.

Keywords*: austenite, martensite, EBSD, sample preparation.*

1. Introduction

Martensitic steel is one of the most widely used iron base structural materials with the most outstanding mechanical properties. Besides Fe it consists of carbon varying between a few hundredths to a few tenths of a percent by weight and a variety of different alloying elements in small quantities. It is produced by fast cooling from a temperature where the fcc austenitic γ phase is stable to around room temperature, where the bcc α phase is stable. All physical properties depend on the alloy composition, but principally on carbon content and cooling characteristics. The speed of cooling from the austenite state and the carbon content are the main factors determining the microstructure and the mechanical properties of martensitic steels [1].

One possible form of martensite is the so called lath martensite. A typical lath martensite consists of blocks of lamellar plates where the blocks form packets [2–4]. The blocks are further subdivided into sub-blocks, where the smallest constituents of the structure are the lamellar plates called martensite-laths. The hierarchical structure of packets, blocks, sub-blocks and laths in lath martensite is shown schematically in Figure 1.

Within the prior austenite grain boundary several packets of different crystallographic orientations can coexist [2–4], as shown in Figure 1.

Despite the rather large elastic limit of martensitic steels they do show some ductility [1, 5–7]. There have recently been attempts to reveal the microscopic mechanism controlling plastic deformation in lath-martensite, by microscale deformation experiments [8–9].

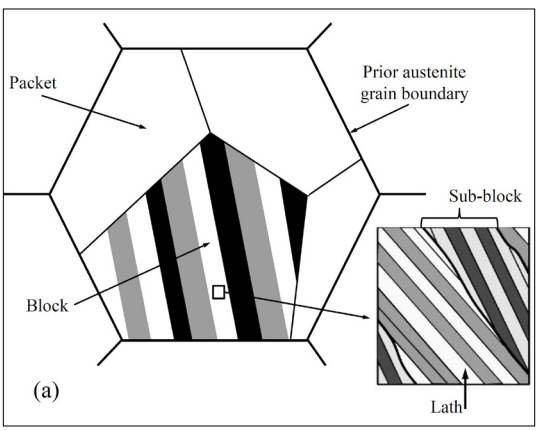

Figure 1. *The hierarchical structure of packets, sub-blocks, blocks and lath in lath martensite.*

Micropillars with a single martensite block have shown perfectly ideal stress-strain behaviour with no strain hardening and a flow stress of 1.2 GPa. Micropillars with two or more blocks, however, have shown significant strain hardening with a similarly large elastic limit [8].

Tensile experiments on microscale specimens of lath martensite of the order of 100 μm length showed that the critical-resolved-shear-stress (CRSS) was relatively small, of the order of 350 MPa, when the active slip systems were in-lath-plane, whereas the CRSS was almost doubled when the active slip systems were out-of-lath-plane [9].

The two experiments in [8, 9] indicate that there may be a load redistribution between packets in which the active slip systems are in- or out-of-lath-plane. Two packets oriented with the active Burgers vectors either in- or out-of-lath-plane relative to the direction of the applied stress, σ, are shown schematically in Figure 2.

The different elastic-plastic response is brought about solely by the different crystallographic orientation of the two packets relative to the direction of σ. As a result, the plastic deformation creates a composite in which the packets with active Burgers vectors in-lath-plane become the soft, whereas those with active Burgers vectors out-of-lath-plane become the hard components.

This short introduction shows how important it is for our research that we are able to examine the orientation of packets and those relationships with directions of stress which cause of plastic deformation. We use electron backscatter diffraction (EBSD) to achieve this. EBSD examination requires very careful sample preparation. In our work we have developed a sample preparation method for electron backscatter diffraction examination.

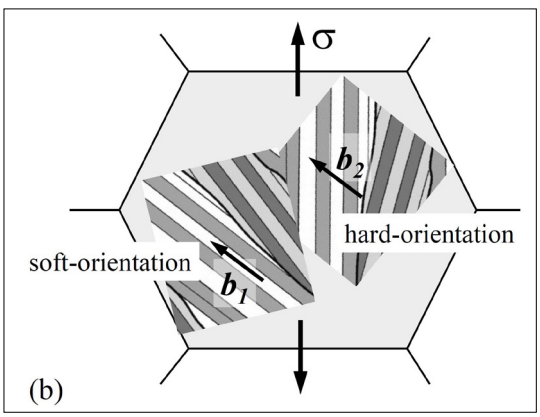

Figure 2. *Two packets oriented with the active Burgers vectors either in- or out-of- lath plane relative to the direction of the applied stress*

2. Materials and methods

The samples were used for our measurements with edge lengths of $l_1 = 20$ *mm* and $l_2 = 20$ *mm* and a thickness of $h = 2.5$ *mm*. The material composition of the specimens is summarized in Table 1. The material composition of the specimens was measured using a Zeiss Evo MA 10 Scanning Electron Microscope (SEM).

The samples were heated to 1100 °C (this is above the temperature of steel A3) and then held for 30 min followed by water cooling down to 20 °C. This way, we could product lath martensite.

In the next step, the specimens were embedded in an electrically conductive hot embedding resin. This is an important step because both EBSD and ion polisher can examine well only conductive samples, so there is no need to take out the specimens from the resin and risk them in this way possible injuries.

The next step was mechanical grinding and polishing with different Silicon carbide (SiC) and diamond particle size sandpapers (SiC particle sizes: 300 μm, 212 μm, 90 μm, 46 μm, 26 μm, 15 μm, 12 μm, 6 μm; diamond particle sizes: 3 μm, 1 μm). All types of grinding paper were used for 5 minutes and all types of polishing paper were used for 10 minutes. At this point, all of the specimens were prepared in the same way, but this is insufficient for EBSD measurements. For better results, the specimens were ionpolished with a Technoorg Linda SEM Prep2 ionpolisher. The task may seem easy at first, but accurate adjustment of many variables (anode voltage, anode current, milling angle, sputtering time, ion source) is required for proper sample preparation. Two of the variables were changed during the measurement, one of them – the milling angle – was changed from 10 to 110, the other variable was the sputter time, this was increased from 1 hour to 6 hours.

Table 1. *Material composition of our specimens.*

Element	Weight %
Fe	98.10
C	0.21
Mn	1.58
P	0.03
S	0.04
Si	0.04

The other variables were set to the following values: anode voltage: 10 kV, anode current: 3.5 A, beam current: 2 mA, ion: Ar+.

After the samples were prepared, we performed EBSD measurements. From the measurements, we obtain IQ (image quality) maps which are used to determine the quality of image from electron backscattered diffraction examination.

The higher the IQ value, the better the obtained result. Our goal is that the IQ value exceeds 40,000 because the results obtained above this are already correct.

3. Results

First, we established the ideal milling angle. Each sample was ionpolished for 1 hour. The IQ values for each milling angle were plotted in the following diagram (**Figure 3**) .

As we can see in the diagram, the ideal milling angle is 70. After this, only the sputter time was modified and the milling angle was set at 70. The result can be seen in the **Figure 4.**

As we can see in the diagram, the ideal sputtering time was 4 hours, but the average IQ value was over 40 000 at 3 and 5 hours. Based on this, we can say the best ion polishing parameters are:

- anode voltage: 10 kV,
- anode current: 3.5 A,
- beam current: 2 mA,
- ion: Ar^+,
- sputtering time: 4 h,
- milling angle: 7°.

An IQ map of a sample made with these parameters in **Figure 5.**

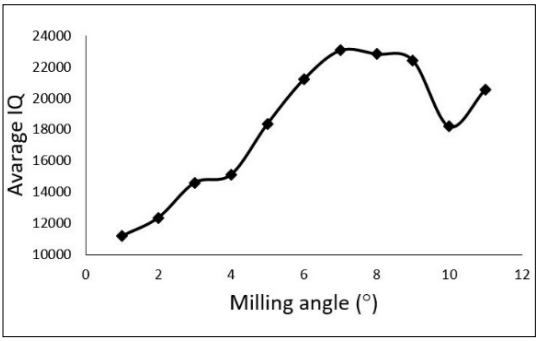

Figure 3. *Average IQ values of EBSD measurement of our steel specimens as a function of the milling angle of the samples, where the sputtering time was 1 hour.*

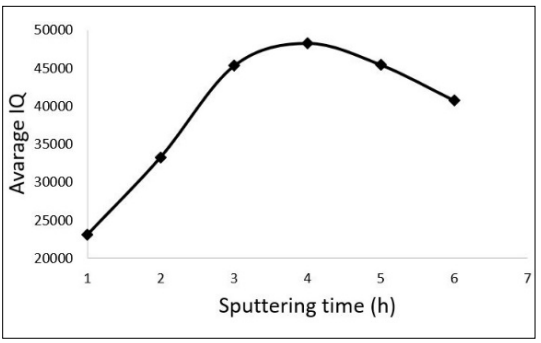

Figure 4. *Average IQ values of EBSD measurement of our steel specimens as a function of the sputtering time of the samples, where the milling angle was 7°.*

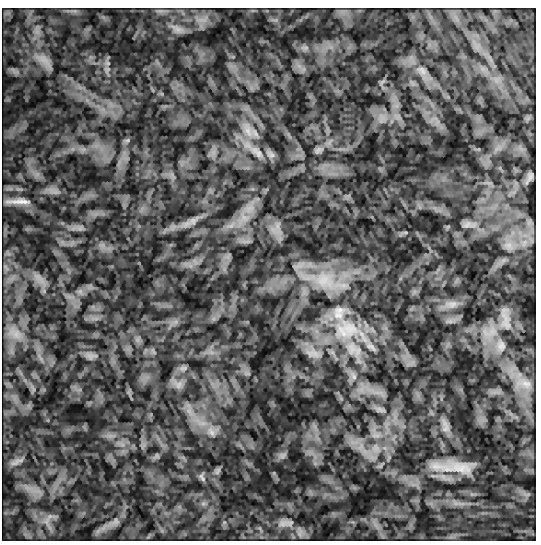

Figure 5. *IQ map of a sample made with best parameters.*

Acknowledgement

The publication of the work reported herein has been supported by the NTP-SZKOLL-19-066 National Talent Programme of the Ministry of Human Capacities, and by the „OTKA" grant K124926 funded by National Research, Development and Innovation Office (NKFIH).

References

[1] Krauss G.: *Martensite in steel: strength and structure.* Material Science and Engineering A, 273-275. (1999) 40–57. https://doi.org/10.1016/S0921-5093(99)00288-9

[2] Krauss G., Mader A. R.: *The morphology of martensite in iron alloys*. Metallurgical Transactions, 2. (1971) 2343–2357. https://doi.org/10.1007/BF02814873

[3] Morito S., Tanaka H., Konishi R., Furuhara T., Maki T.: *The morphology and crystallography of lath martensite in Fe-C alloys*. Acta Materialia, 51. (2003) 1789–1799. https://doi.org/10.1016/S1359-6454(02)00577-3

[4] Kitahara H., Ueji R., Tsuji N., Minamino Y.: *Crystallographic features of lath martensite in low-carbon steel*. Acta Materialia, 54. (2006) 1279–1288. https://doi.org/10.1016/j.actamat.2005.11.001

[5] Swarr T., Krauss G.: *The effect of structure on the deformation of as-wuenched and tempered martensire in an Fe-0.2 pct C alloy*. Metallurgical Transactions A, 7/1. (1976) 41–48. https://doi.org/10.1007/BF02644037

[6] Michiuchi M., Nambu S., Ishimoto Y., Inoue J., Koseki, T.: *Relationship between local deformation behavior and crystallographic features of as-quenched lath martensite during uniaxial tensile deformation*. Acta Materialia, 57. (2009) 5283–5291. https://doi.org/10.1016/j.actamat.2009.06.021

[7] Nambu S., Michiuchi M., Ishimoto Y., Asakura K., Inoue J., Koseki T.: *Transition in deformation behaviour of martensitic steel during large deformation under unaxial tensile laoading*. Scripta Materialia, 60. (2009) 221–224. https://doi.org/10.1016/j.scriptamat.2008.10.07

[8] Ghassemi-Armaki H., Chen P., Bhat S., Sadagopan S. Kumar S., Bower A.: *Microscale-calibrated modeling of the deformation response of low-carbon martensite.* Acta Materialia, 61. (2013) 640–3652. https://doi.org/10.1016/j.actamat.2013.10.001

[9] Mine Y., Hirashita K., Takashima H., Matsuda M., Takashima K.: *Micro-tension behaviour of lath martensite structures of carbon steel*. Material Science and Engineering A, (2013) 535–544. https://doi.org/10.1016/j.msea.2012.09.099

sciendo

Acta Materialia Transylvanica 3/2. (2020) 94–97.
DOI: hungarian: https://doi.org/10.33923/amt-2020-02-08
english: https://doi.org/10.33924/amt-2020-02-08

ACTA MATERIALIA TRANSYLVANICA

Development of Microfluidic Cell for Liquid Phase Layer Deposition Tracking

József Bálint RENKÓ,[1] Attila BONYÁR,[2] Péter János SZABÓ[3]

Budapest University of Technology and Economics, Department of Materials Science and Engineering, Budapest, Hungary

[1] *renko.jozsef@edu.bme.hu*

[2] *bonyar@ett.bme.hu*

[3] *szpj@eik.bme.hu*

Abstract

This paper shows how microfluidic tools can be used for up-to-date microstructural investigations based on thin film deposition. The construction and production methods of such measuring procedures are introduced, and their application in ellipsometric investigations is shown. By using these tools, the researchers provide the possibility to observe and document the effects of certain fine structural processes in the development of the final microstructure. This paper describes two specific application areas of such microfluidics cells. Microfluidics cells can be used together with both optical microscopy and spectroscopic ellipsometry to understand previously unexplored microstructural changes.

Keywords*: microfluidics, material science, rapid prototyping, in situ material testing.*

1. Introduction

Nowadays with the advancement of technology the quality of produced materials has begun to improve significantly. As a result, there has been a growing need for advanced material testing methods [1]. However, some of the currently used manufacturing and material testing methods still contain procedures for which the process of the occurring phenomena is not yet fully understood.

A good example of this phenomenon are the different etching processes, especially colour etching. In optical microscopic analysis etching is a common method for revealing the microstructure of previously polished specimens [2]. Despite its frequent use, many microstructural changes during etching have not been fully explained [3], although many attempts have been made to clarify the connection between colour etching and certain metallographic properties [4, 5].

Due to the extensive use of rapid prototyping methods and to the development of polymer materials, a new possibility to monitor microstructural changes has emerged. Additive manufacturing technologies have now achieved the dimensional accuracy needed to create channels up to a few tens of millimeters in diameter [6]. Using these techniques and materials, microfluidic cells can be formed in which the etchant can be circulated under controlled conditions [7]. Depending on the design of the cell, microfluidics may be combined with devices already used in metallography, such as an optical microscope or a spectroscopic ellipsometer. Thus, the etching processes could not only be investigated in discrete moments but also in situ.

2. Experimental

2.1. Design of microfluidic cells

To demonstrate the versatility of the fabrication methods, two different cells have been designed.

When designing the microfluidic cells, care must be taken to ensure that the completed system can be integrated into the equipment to be used with it. For a cell-compatible geometry, the sample had to be embedded so that it could be examined independently of its original geometry.

The first microfluidic cell was designed to be compatible with an optical microscope. This enables real-time optical tracking of etching and layer-building processes [8].

As the magnification increases, the working distance between the objective and the specimen becomes smaller. Thus, the maximum resolution had to be considered during the design. An Olympus BX51 type LMPlan FI50/0.50 long working distance optical microscope with a minimum focal length of 3.6 mm was selected as an equipment to be designed for. The laminar flow of the etchant is provided by the formed channel system, supported by syringe pumps. Since good quality images require a sufficiently long distance between the objective of the microscope and the sample, the cell is closed as shown in Figure 1 by a glass sheet. The design considerations are also illustrated in Figure 1. There is another chamfer in the finished geometry for the junction between the sample and the cell, which makes it easier to swap the samples (Figure 2).

The second microfluidic cell was specifically designed to be used with a spectroscopic ellipsometer. Ellipsometry enables the measurement of surface layer thickness with nano meter accuracy, to study optical refractive index, homogeneity or even the surface's nano roughness[9].

Ellipsometry is particularly sensitive to refraction at interfaces. The cell must be designed so that the beam of light used for the test passes through each crossing interface perpendicular to the surface of the sample. Thus, maximal luminous intensity and low noise can be ensured. For designing the cell, a Woollam M-2000DI ellipsometer was used. The beam of light exiting the transmitter is approximately 3 mm in diameter, decreasing to one-tenth until it reaches the sample's surface. (Figure 3).

A moving mechanism must be also provided which allows the beam to be focused at any point on the surface to be examined, while the sample is fixed. Therefore, the microfluidic cell must be created from two parts. The upper cell provides the flow of the etchant and the angles required for the maximal intensity. The lower cell is used to fix and position the specimen. The two halves can be attached to each other as shown in Figure 4.

2.2. Fabrication of the microfluidic cells

To create microfluidic cells, a chemically inert material that does not react with either the sample or the etchant should be chosen. The material also must be transparent to let the light pass through. Poly-dimethyl-siloxane (PDMS) was chosen as the base material of the cells. It has an already proven quality for microfluidic cell manufacturing. When the monomer of PDMS is mixed with the curing agent in a 10:1 ratio, the high viscosity mixture begins to crosslink. This mixture was filled into a mould, then heat treated at 100 °C for 60 minutes to support polymerisation. The moulds for both cells were made with an Objet Eden 250 type 3D printer.

The created PDMS cell which is compatible with an optical microscope is bonded onto a glass sheet by crown discharge treatment to seal the cell. To strengthen the bond, the finished cell was pressed on the glass sheet and rested in an oven at 60 °C for an additional 30 minutes. The internal channel system of the cell thus formed has a volume of 205 mm^3 (Figure 5).

In the case of the other cells created to be used with an ellipsometer, the glass sheet could not provide the perpendicular angle of light entry

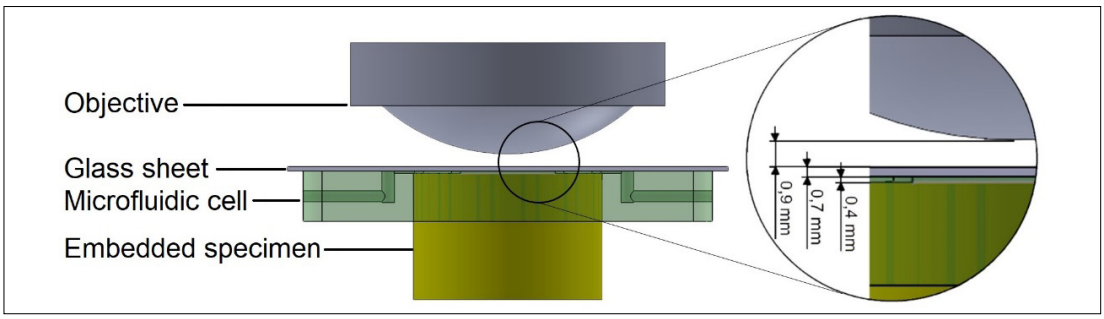

Figure 1. *The dimensions of the microfluidic cell, which is compatible with an optical microscope.*

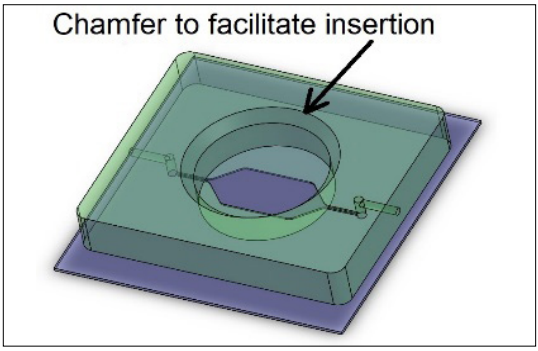

Figure 2. *3D design of the microfluidic cell which is compatible with an optical microscope.*

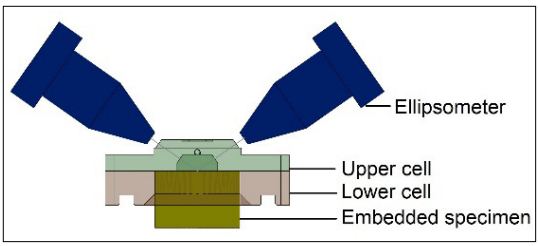

Figure 3. *Design of microfluidic cell compatible with spectroscopic ellipsometer.*

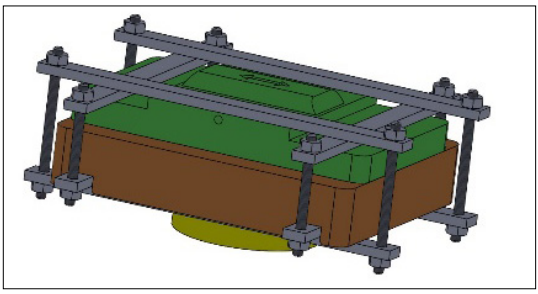

Figure 4. *Clamping mechanism of microfluidic cell which is compatible with an ellipsometer.*

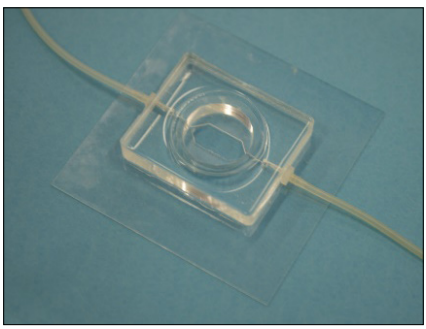

Figure 5. *The fabricated microfluidic cell which is compatible with an optical microscope. Silicone tubes are attached to both ends of the cell.*

and exit. Thus, both the top and bottom of the cell should be made by PDMS. They can be secured to each other as shown in **Figure 4.** This cell has an internal channel volume of 851 mm^3.

3. Application of microfluidic cells

The inlet and outlet openings of the cell can be connected to a syringe pump by means of silicon tubes. The pump can supply the cell with fresh etchant while the laminar flow is ensured. The equipment thus developed is able to track the processes on the sample's surface by various means throughout the etching process. The technique allows digital image capture for the first presented cell and the following of interference change caused by layer growth on the sample surface for the second cell.

Although the use of microfluidics systems extends the capabilities of microstructure testing methods, the limitations of the system should not be forgotten. In microscopic examinations, the magnitude of magnification cannot be increased indefinitely due to the focal length of the used lens. The smallest particle size that can be examined is approximately 3–5 μm. For the other microfluidic cell, developed for ellipsometry, the dimensions of the internal channels of the cell are bound to provide light paths, so that the entire volume must be filled with the desired milling agent prior to measurement. Because the microfluidics system takes time to fill, the initial etching phase cannot be recorded..

4. Conclusion

Microfluidic systems enable in situ microstructure investigations, which could significantly improve the monitoring of etching and thin-layer growth processes. Despite the obvious drawbacks of the technology, it is well suited to combine with other microstructure analysing equipment. Furthermore, they can be safely used in corrosion, etching, or coating applications due to their closed system.

Acknowledgement

This paper was supported by the ÚNKP-19-3-I-BME-266 New National Excellence Program of the Ministry for Innovation and Technology.

The publication of the work reported herein has been supported by the NTP-SZKOLL-19-066 National Talent Programme of the Ministry of Human Capacities.

References

[1] Leuders S., Thöne M., Riemer A., Niendorf T., Tröster T., Richard H. A., Maier H. J.: *On the Mechanical Behaviour of Titanium Alloy TiAl6v4 Manufactured by Selective Laser Melting: Fatigue Resistance and Crack Growth Performance*. International Journal of Fatigue, 48. (2013) 300–307. https://doi.org/10.1016/j.ijfatigue.2012.11.011.

[2] Beraha E.: *New Metallographic Reagents for Stainless Steel and Heat-Resisting Alloys*. J. Iron Steel Inst., March (1966), 248–251.

[3] Schaberger E., Grote F., Schievenbusch A.: *Colour Etching and Coloured Image Analysis – A Way of Characterising the Microstructures of Innovative Cast Materials*. Praktische Metallographie/Practical Metallography, 37. (2000) 419–434.

[4] Bonyár A., Szabó P. J.: *Correlation Between the Grain Orientation Dependence of Color Etching and Chemical Etching*. Microscopy and Microanalysis, 18/6. (2012) 1389–1392. https://doi.org/10.1017/S1431927612013554

[5] Szabó P. J., Bonyár A.: *Effect of Grain Orientation on Chemical Etching*. Micron, 43/2–3. (2012) 349–351. https://doi.org/10.1016/j.micron.2011.09.015

[6] Takagishi K., Umezu S.: *Development of the Improving Process for the 3D Printed Structure*. Scientific Reports, 7. (2017) art. 39852. https://doi.org/10.1038/srep39852

[7] Bonyár A., Sántha H., Ring B., Varga M., Kovács J. G., Harsányi G.: *3D Rapid Prototyping Technology (RPT) As a Powerful Tool in Microfluidic Development*. Procedia Engineering, 5. (2010) 291–294.

[8] Bonyár A., Renkó J., Kovács D., Szabó P. J.: *Understanding the Mechanism of Beraha-I Type Color Etching: Determination of The Orientation Dependent Etch Rate, Layer Refractive Index and a Method for Quantifying the Angle Between Surface Normal and the ‹100›, ‹111› Directions for Individual Grains*. Materials Characterization, 156. (2019) 109844. https://doi.org/10.1016/j.matchar.2019.109844

[9] Fodor B., Defforge T., Agócs E., Fried M., Gautier G., Petrik P.: *Spectroscopic Ellipsometry of Columnar Porous Si Thin Films and Si Nanowires*. Applied Surface Science, 421. Part B (2017) 397–404. https://doi.org/10.1016/j.apsusc.2016.12.063

sciendo

Acta Materialia Transylvanica 3/2. (2020) 98–102.
DOI: hungarian: https://doi.org/10.33923/amt-2020-02-09
english: https://doi.org/10.33924/amt-2020-02-09

ACTA MATERIALIA TRANSYLVANICA

Damage Analysis of Broken Orthopedic Implants

Ágota SIMON,[1] Lilla ASZTALOS[2]

Budapest University of Technology and Economics, Department of Materials Science and Engineering, Budapest, Hungary

[1] *simon_agota@yahoo.com*

[2] *lilla@eik.bme.hu*

Abstract

Joint implants and fixings are subject to many stresses throughout their life cycle. Despite careful design, material selection, manufacturing technology and proper surgical technology, implant damage and, in extreme cases, fracture can occur. Investigation of injuries is important from the perspective of the patient, the care provider and the manufacturer, among other things, by exploring the cause of the fracture to prevent similar cases. In the present study we performed failure analysis of a hip implant and a bone fixation plate. Fracture surfaces, material composition, material structure and hardness were also investigated. Based on the work done, we determined what might have led to the fracture in both cases.

Keywords*: hip implant, bone fixation, fracture, damage analysis.*

1. Introduction

Joint diseases today are considered to be common diseases. Such diseases include a decrease in bone density with age and abrasion. A decrease in bone density can result in a fracture of the bone, and abrasion disease primarily affects the vertebrae and hip joints due to the vertical position of the body. The femoral head and the inner surface of the acetabulum are the articular cartilage itself, which allows the surfaces of the two bones to slide on each other without injury. The joint is held stable by muscles and tendons **[1, 2]**.

The most effective treatment for advanced hip disease is full joint replacement with a hip implant. These implants can be made of different materials and the way they are implanted can be different. Age and the patient's lifestyle will best determine which technique and implant the doctor chooses for the patient **[1, 2]**.

In the case of the femur suffering a fracture, another device is needed to repair the bone and joint. In this case, a bone fixation plate is used. The plate is fixed to the broken bone fragments with screws, and the screwing method can be compression or neutral **[3]**.

1.1. Failure of hip implants

Orthopedic implants can have a life expectancy of up to 30 years, but hip implants require replacement or revision of the implants every 10-15 years or sooner to prevent or treat abrasion, modular head wear and implant loosening **[4–7]**.

Implants are exposed to various effects after implantation, such as mechanical stress and friction, but even during surgery, there may be factors that reduce the life of the implant. In these cases, the patient can return to the treating doctor with complaints within a few years. Decreased bone density can also be a factor in damage to the prosthesis, as the bone structure is no longer able to maintain the stability of the implant **[5]**.

The success of the implantation is influenced by the surgical technique as to whether the fixation was done at the right angle and extent. In addition to the implant itself and the surgery, the patient also plays an important role in maintaining the condition of the implant, following the instructions of the manufacturer and the physician **[4, 6]**. There are cases where the accident to the patient is the cause of the injury, but even prolonged exposure may be the cause, such as, for

example, the pain of the opposite hip and the consequent incorrect gait pattern [7, 8].

Types of damage are usually fracture, abrasion, loosening, and sprain as well [4–8]. Of these, the most severe case that most affects a patient's quality of life is fracture. To find out what was behind the fracture, failure analysis should be performed on the damaged samples.

1.2. Failure analysis of broken implants

As the impairment can lead to a significant deterioration in the patient's quality of life, all cases should be investigated. Numerous articles in the literature also report case studies [4–8], but they also try to go around the topic as accurately as possible by finite element modelling of the use of hip implants [9]. Most articles focus on the medical side, but article scan also be found on the metallographic and corrosion properties of damaged metal [10, 11].

In recent years, the Department of Materials Science and Technology at Budapest University of Technology and Economics has investigated the damage of several broken hip implants. These measurements were also the basis of our present research.

2. Methods

The aim of our research is to perform failure analysis of two broken implants and to reveal the cause of the damage. One of the implants examined is a hip prosthesis (Figure 1), that has ruptured at the stem, and the other device is a bone fixation plate (Figure 2). In the case of the bone fixation plate, fixation screws were also available, on which no traces of fracture were detected macroscopically, but they were also examined in order to fully evaluate the damage.

Figure 1. *The distal part of the broken hip implant.*

Figure 2. *Distal part of the broken bone fixation plate.*

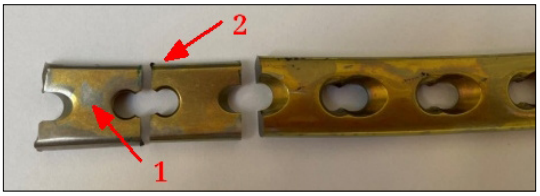

Figure 3. *The distal part of the bone fixation plate after dissection. Slice with fracture surface number 1, number used for metallographic and hardness tests 2.*

2.1. Specimen preparation

Macroscopic images of the damaged implants were taken at the time of receipt, followed by ultrasonic cleaning. In order to properly examine the fracture surfaces of the implant, the implants were dissected at a distance of 10 mm from the fracture line. In order to examine both the hardness and the fabric structure of the material, additional slices were cut parallel to the fracture line (Figure 3).

2.2. Fractography

The removed fractures were imaged with a stereomicroscope (Olympus SZX16) at different magnifications. However, with this method, we have not yet been able to determine the exact cause of the fracture.

Fracture surfaces were then scanned at higher magnifications using a scanning electron microscope (Zeiss EVO MA 10). Scanning the edge of the fracture surfaces along the surface, we looked for crack lines starting from the surface as well as material continuity deficiencies that may have played a role in the damage.

2.3. Metallography

To perform the measurements, the pieces cut from the implants were embedded, then polished. The polished surfaces were imaged with a metallurgical microscope showing the micro-structural features (precipitations, grain size, etc.). By etching the polished patterns, the fabric structure also becomes visible. Kroll's reagent (92 mL H_2O, 6 mL HNO_3, 2 mL HF) was used for the plate and the fixing screw, and hydrochloric acid was used for the hip implant. Microscopic images can also be used to determine the average particle size and the homogeneity of the particle structure.

2.4. Material composition analysis

Material composition analysis was performed on both the fracture surface and the prepared

abrasives by energy dispersive X-ray spectrometry (Edax Metek Elect Plus). Material composition tests can be used to identify the material of the implants and to compare the values with those specified in the standard. The material composition of precipitates and inclusions identified in previous studies can also be analysed with this method.

2.5. Hardness testing

The final step in investigating the damage cases investigated in the current research was the hardness test of the implant material. The specimens prepared for metallographic examination were subjected to HV1 hardness measurements (Bühler 1105) on the surface of the specimens transversely and longitudinally, starting from the edge of the specimen at 1 mm intervals. The hardness results are also comparable to those specified in the standard, and any inhomogeneities can be detected by measuring the entire cross-section.

3. Results

3.1. Visual testing, macro- and micro-fractography

As a result of visual inspection, small and large surface scratches and injuries were clearly visible on the surfaces of the implants. These are presumably generated during removal and are not associated with damage. In the case of the plate, the wear of the anodized layer was conspicuous (**Figures 2**, **3**).

The characteristics of fatigue fracture could be clearly seen on the surface of the samples. Bone cortex remains were not wedged on the fracture surface. In the case of the fixing plate, crack lines starting from the screw thread could be observed (**Figure 4**). From the surface of the stems, it can be assumed that the fracture was a longer process, the two stems did not break at the same time. On the surface of one stem of the plate there is a plastic deformation due to prolonged impact of the material, while on the other part of the stem the crack propagation characteristic of fatigue fracture is not visible, but rather indicates a brittle fracture. (**Figure 5**).

In the case of the prosthesis, several cracks could be observed on the fracture surface that ran to the surface (**Figure 6**). In this case, too, we thought we would discover the characteristics of a fatigue fracture.

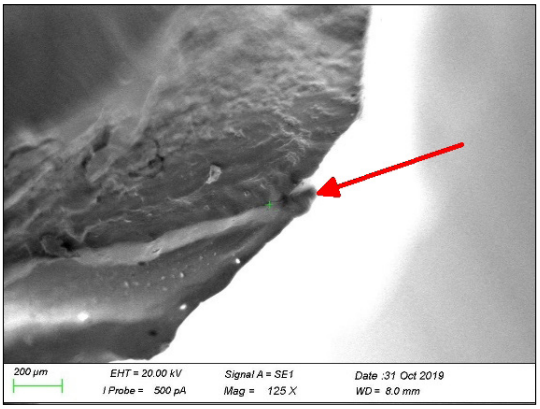

Figure 4. *In this case, too, we thought we would discover the characteristics of a fatigue fracture.*

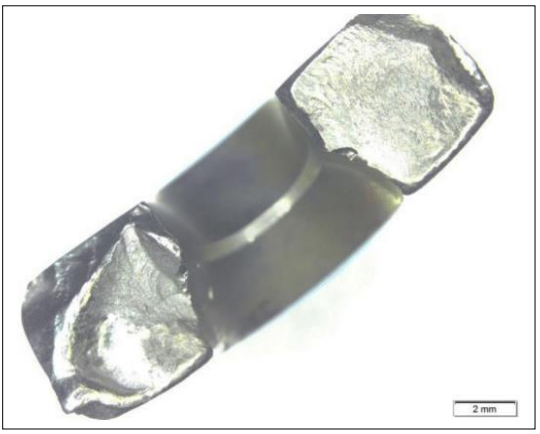

Figure 5. *Stereomicroscopic image of the fracture surfaces of the bone fixation plate.*

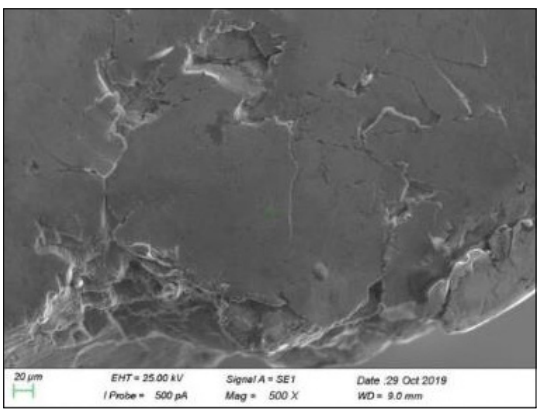

Figure 6. *Electron microscopic image of the fracture surface of the hip implant. Multiple cracks can be observed at the surface edge.*

3.2. Metallography

Metallographic examination of the plate revealed that it had a fine-grained, homogeneous grain structure, containing fine and well-dispersed precipitates, which improve significantly the strength (**Figure 7**). The screw securing the plate was also subjected to metallographic examination. The grain structure was the same as the plate structure.

The granular structure of the hip implant was dendritic, which is not conducive to the propagation of cracks (**Figure 8**). On the electron micrographs, we observed that the fracture lines ran between the dendritic spikes.

In terms of material composition, the fixing plate and the associated screw are made of Ti-Al-Nb alloy and the hip implant is made of cobalt-chromium alloy.

During the hardness measurement, no outliers were obtained for any of the implants. For the plate, the values fell in the 300 HV range. The average of the measurements was 300.5 HV, which corresponds to the value of the relevant standard (ISO 5832-11) (32 HRC = 300 HV). The screw hardness values for the plate ranged from 305.6 to 316.9 HV, averaging 309.62 HV. Hip prosthesis values ranged from 303.2 to 348.9 HV. Its average was 327.75 HV, which also corresponded to the value specified in the standard (ISO 5832-4) (33 HRC = 311 HV).

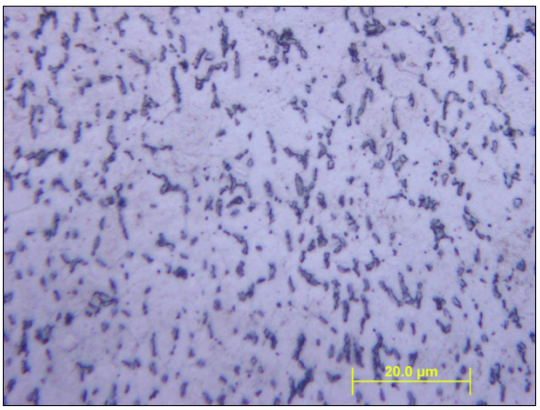

Figure 7. *Microstructure of the bone fixation plate; it shows the fine and dispersed precipitates.*

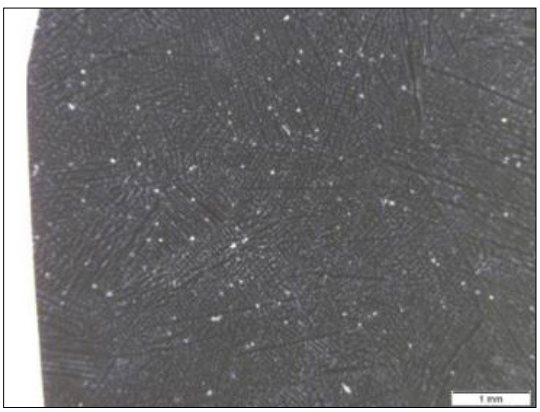

Figure 8. *Dendritic micro-structure of the cast material of the hip implant.*

4. Conclusions

In the case of the fixing plate, the cracks that started the fracture came from the screw surface. From the fracture surface, it can be concluded that the two parts did not break at the same time, as a large amount of plastic deformation could be observed on one of the stems, which can be attributed to the continuous collision of the fracture surfaces. The cause of the fracture may have been a scratch caused by a piece of bone, or even excessive tightening of the screw. In the case of the hip implant, the cause of the fracture is unknown. Cracks running to the surface may have been a possible starting point for the fracture. Even during surgery, the surface may have been damaged, causing the implant to break in the long run.

The material composition and hardness of the tested devices complied with the standards, but our research revealed factors that may have reduced the resistance of the given structure to fracture and could lead to premature damage to the implant.

References

[1] Sargeant A. et al.: *Hip implants: Paper V. Physiological effects.* Materials & Design, 27/4. (2006) 287–307. https://doi.org/10.1016/j.matdes.2004.10.028

[2] Derar H. et al.: *Recent Patents and Designs on Hip Replacement Prostheses.* The Open Biomedical Engineering Journal, 9. (2015) 92–102. https://doi.org/10.2174/1874120701509010092

[3] Krettek C. et al.: *Evolution of Minimally Invasive Plate Osteosynthesis (MIPO) in the femur).* International Journal of the Care of the Injured, 32/3. (2001) 14–23. https://doi.org/10.1016/S0020-1383(01)00180-2

[4] Martens M. et al.: *Factors in the Mechanical Failure of the Femoral Component in Total Hip Prosthesis: Report of Six Fatigue Fractures of the Femoral Stern and Results of Experimental Loading Tests.* Acta Orthopaedica Scandinavica, 45/5. (1974) 693–710. https://doi.org/10.3109/17453677408989679

[5] Carlsson A. S., et al.: *Fracture of the femoral prosthesis in total hip replacement according to charnley.* Acta Orthopaedica Scandinavica, 48/6. (1977) 650–655. https://doi.org/10.3109/17453677708994812
[6] Collins D. K. et al.: *Femoral stem failure in total hip replacement*. Journal of Bone and Joint Surgery A, 69/8. (1977) 1033–1041.
[7] Wilson L. F. et al.: *Fracture of the femoral stem of the ring TCH hip prosthesis.* Journal of Bone and Joint Surgery B, 74/5. (1992) 725–728. https://doi.org/10.1302/0301-620X.74B5.1527122
[8] Lizano-Diez X. et al.: *Fracture of the femoral component after a lightning strike injury: A case report*. Acta Orthopaedica et Traumatologica Turcica, 51/1. (2017) 84–87. https://doi.org/10.1016/j.aott.2015.04.001
[9] Srimongkol S.: *A review of mathematical modelling in total hip replacement*. International Mathematical Forum, 7/52. (2012) 2561–2569.
[10] Godec M.: *Material failure of an AISI 316l stainless steel hip prosthesis.* Materiali in Tehnologije, 45/2. (2011) 85–90. http://mit.imt.si/izvodi/mit112/godec.pdf
[11] Collier J. P. et al.: *Corrosion between the components of modular femoral hip prostheses*. Journal of Bone and Joint Surgery B, 74/4. (1992) 511–517. https://doi.org/10.1302/0301-620X.74B4.1624507

sciendo

Acta Materialia Transylvanica 3/2. (2020) 103–107.
DOI: magyar: https://doi.org/10.33923/amt-2020-02-10
angol: https://doi.org/10.33924/amt-2020-02-10

ACTA MATERIALIA TRANSYLVANICA

Effect of Heat Treatment on the Microstructure of Duplex Stainless Steel Welds

Ferenc TOLNAI,[1] Balázs VARBAI[2]

Budapest University of Technology and Economics, Faculty of Mechanical Engineering, Department of Materials Science and Engineering, Budapest, Hungary

[1] *ferenctolnai1@gmai.com*

[2] *varbai@eik.bme.hu*

Abstract

Duplex stainless steels (DSS) are gaining in popularity due to their characteristic features, excellent mechanical properties, and corrosion resistance. The microstructure of DSSs consists of ferrite up to 50 %, and the rest is built up from austenite. The ferritic microstructure can cause chromium-nitride precipitation because the nitrogen solubility in the ferrite phase is very low below 700 °C. Our research showed that electrochemical etching is an acceptable process for revealing chromium-nitrides. Additionally, our research points out that chromium-nitride acts as a secondary austenite nucleation site.

Keywords*: heat treatment, duplex stainless steels, austenite, electrochemical etching, nitrogen.*

1. Introduction

Duplex stainless steels provide a high-strength alternative to design engineers within the family of stainless steels. However, the welding of duplex steels requires extreme attention and precise observance of technological variables due to the formation of many possible non-equilibrium transformations [1, 2]. To maintain the appropriate 1:1 austenite (γ):ferrite (δ) phase ratio and alloy content, a usually nickel-over alloyed filler material or nitrogen-containing shielding gas, is recommended for the welding of duplex steels [3–4].

Duplex steels are also alloyed with nitrogen (N) because N is an austenite-forming element, which is more soluble in austenite than in ferrite [5]. Therefore, when the delta-ferrite cools from 1100 °C, it becomes supersaturated in nitrogen, resulting in chromium nitride precipitations (Cr_2N). Chemical composition, cooling rate, and ferrite grain size are factors that determine which precipitates appear. Nitrogen-containing shielding gas also plays a significant role in the formation of the austenite phase, so less nitrogen remains in the ferrite phase, and, as a result, less Cr_2N is formed. Secondary austenite (γ_2) is rapidly formed by various temperature-dependent mechanisms [6]. At temperatures between 600 and 800 °C, where diffusion is faster, Widmannstätten-type austenitic phases are formed [6]. Although the N content of the γ_2 phase is higher than that of ferrite, its Cr and Ni contents remain substantially below that of austenite formed from ferrite [6]. In the temperature range of 700–900 °C, another variant of γ_2 appears at the δ/γ phase boundary, which is lower in terms of Cr content [6]. In the present study, we investigated the formation of chromium nitride and secondary austenite phases in the case of TIG welding without filler metal and during post-weld heat treatment.

2. Materials and methods

2.1. Base materials

The base material used for both tungsten inert gas welding (TIG welding) and heat treatment was a conventional X2CrNiMoN22-5-3 (1.4462) duplex steel in the form of a 6 mm thick plate. The chemical composition given by the manufacturer is shown in Table 1.

Table1. *Chemical composition of 1.4462 steel according to the manufacturer's data sheet (%).*

Cr	Ni	Mn	Mo	N	C
22,21	5,76	1,36	3,14	0,164	0,02
Si	**Cu**	**S**	**P**	**Fe**	
0,38	0,30	0,001	0,027	bal.	

2.2. TIG welding and heat treatment

Single-pass butt joints were welded by TIG welding on 200×50×6 mm specimens in the PA (horizontal) position with a welding machine without filler material. Three types of arc energy were used: 0.25 kJ/mm, 0.84 kJ/mm, and 1.57 kJ/mm. These arc energies are in the recommended range of 0.5–2.5 kJ/mm for arc welding of duplex steels [7]. The arc energy was calculated similarly to the heat input, but the thermal efficiency was 1.0. Pure argon (Ar) or 6 % nitrogen shielding gas mixtures (Ar + $6N_2$) were used as shielding gas. The tungsten electrode used in the welding process was 2 % thoriated, 3.2 mm in diameter, with a tip angle of 40°. The automatic welding machine kept the arc length constant at 2 mm in all cases. The shielding gas flow rate was 10 L/min in all cases. The heat treatment was performed in molten salt (50 % NaCl + 50 % KCl) at 800 °C for 10 minutes. The heat treatment was performed only on joints welded with argon shielding gas. The reason for the choice of heat treatment temperature and duration was to observe the formation of the γ_2 phase in the ferritic phase structure.

2.3. Evaluation methods

2.3.1. Microstructure examination

Samples for metallographic analysis were cut with a diamond disk from the welded seam under constant cooling. After cutting, the samples were grinded on 4000 grit sandpaper and then polished with a 3 µm diamond suspension. Metallographic [8] or magnetic [9] examinations can be used to detect austenite and ferrite phases. To calculate the austenite and ferrite phases, Beraha's 2 etchant (85 mL H_2O + 15 mL HCl + 1 g $K_2S_2O_5$) was used, which is suitable for color etching. In images of etched samples, ferrite appears dark, and austenite remains light. To detect possible Cr_2N precipitates, electrochemical etching was performed according to the ISO 17781: 2017 standard. The welded samples were etched in 15 % oxalic acid at 10 V for 10 seconds; this etching method being suitable for the detection of nitride precipitates according to the standard. Oxalic acid etching has previously been successfully used by other researchers to detect carbide and nitride precipitates in ferrite [10, 11], so we also used this electrochemical etching method. The examination of the microstructure was performed with an Olympus PMG-3 optical microscope. Measurement of ferrite content was performed on microstructure images of etched samples taken with an optical microscope, using image analysis software and an area-based method.

3. Results and conclusions

3.1. Microstructure after electrochemical etching

Figure 1 shows a microstructure image after oxalic acid electrochemical etching of the heat-affected zone of the sample welded with 0.25 kJ/mm arc energy and argon shielding gas. It can be seen that oxalic acid electrochemical etching is indeed suitable for the detection of precipitates within the ferrite grain, which are probably chromium nitrides.

The microstructure seen in the images following oxalic acid electrochemical etching shows a similar picture with the results found in the open literature [12–14] These phases have been identified as chromium nitride, so it is likely that in our case, the nitride precipitates were visualized by the applied electrochemical etching. Based on the microstructure analysis following etching, chromium nitride precipitates occurred in the most significant amount in the samples welded with the lowest arc energy, including both shielding

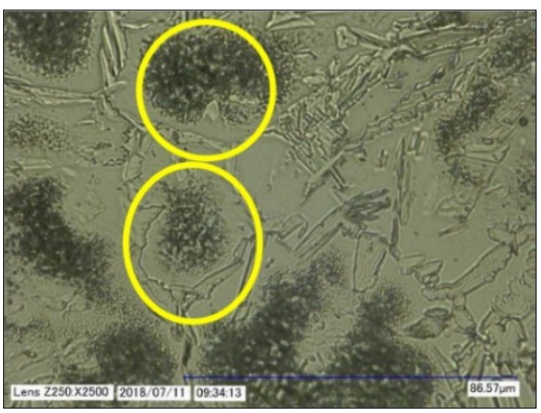

Figure 1. *Possible chromium nitride precipitates inside the ferrite grains in the heat-affected zone. The arc energy was 0.25 kJ/mm, and the shielding gas was argon*

gases used. These nitride precipitates were present inside the ferrite grains and, to a large extent, in the heat-affected zone (Figure 2).

Oxalic acid electrochemical etching, on the other hand, dissolves chromium nitride precipitates, so it was not possible to accurately measure their composition in the present research.

3.2. Microstructure after heat treatment

The heat treatment experiment was performed to achieve the formation of secondary austenite. It can be seen from Figure 3 that the heat treatment applied resulted in an increase in the austenite content in both the weld metal and the heat-affected zone. This is due to the appearance of secondary austenite precipitates in the ferrite particles at the site of the previously observed nitride precipitates. It can also be seen that the formation of secondary austenite started inside the ferrite particles.

Regarding the change in the amount of austenite (Figure 4), it can be observed that the austenite content decreases with increasing arc energy in the case of TIG-welded samples in which pure argon was used as the shielding gas.

The addition of 6 % nitrogen to the shielding gas increased the austenite content of the weld metal because nitrogen is a strong austenite former. In this case, the austenite content of the weld metal is 10% higher than the austenite content of the base materials ~50%.

After the heat treatment of the sample welded with argon shielding gas, the austenite content also increased to 50 %. The increase in the austenite content is the result of the formation of γ_2 in the ferrite grains, in which phase the Cr_2N precipitates that

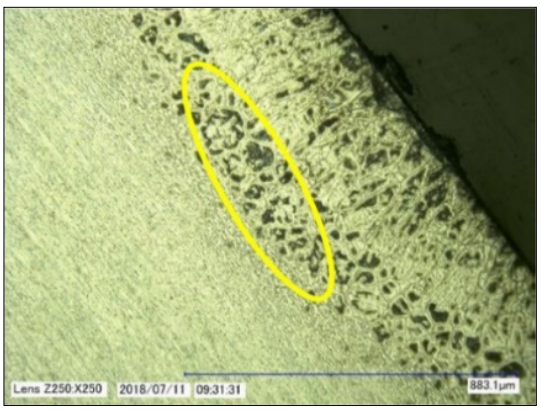

Figure 2. *Possible chromium nitride precipitates inside the ferrite grains in the heat-affected zone. The arc energy was 0.25 kJ/mm, and the shielding gas was argon*

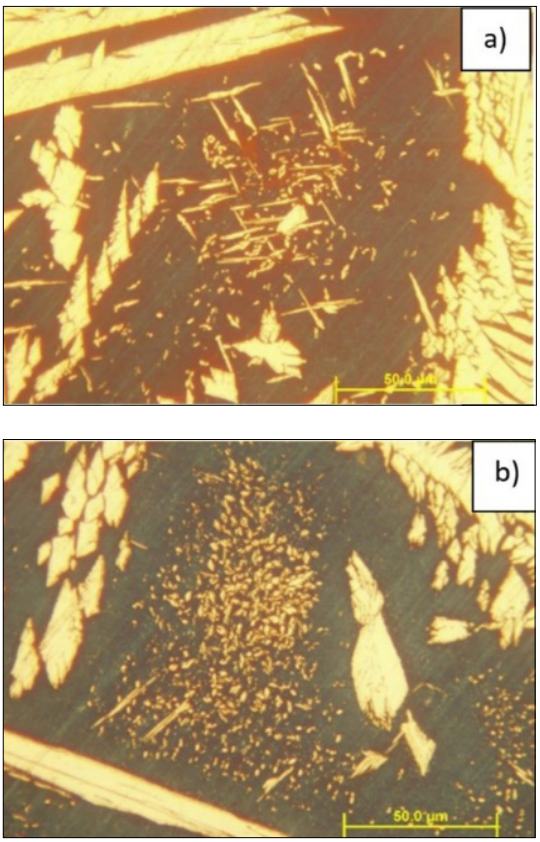

Figure 3. *Microstructure images of the sample welded with argon and the lowest arc energy after heat treatment; (a) weld metal and (b) heat-affected zone*

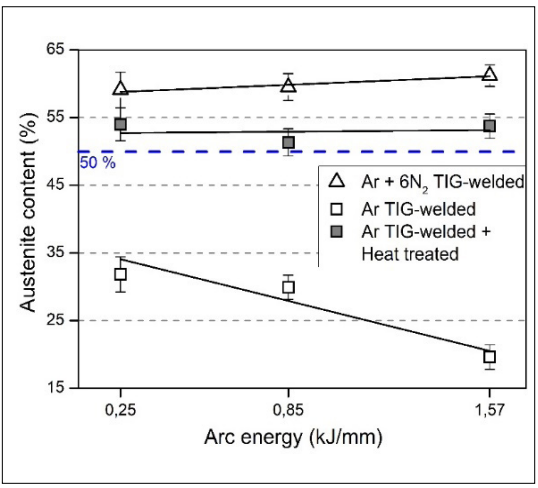

Figure 4. *The austenite content of the weld metal as a function of arc energy, in the case of a sample, welded with both shielding gases and in the case of post-weld heat treatment.*

were present before the heat treatment act as a nucleation site for the formation of the secondary austenite. As the proportion of secondary austenite is high due to heat treatment, we can conclude that γ_2 also plays a very important role in actual, multi-pass welding designs, where it can significantly increase the austenite content of the weld metal during reheating of the previously welded passes [9].

Comparing the results obtained with color etching (Figure 5. a) and electrochemical etching (Figure 5. b), it can be concluded that chromium nitride precipitates led to the formation of secondary austenite in the ferritic heat-affected zone, which is in agreement with the results of other researchers [14].

The formation of secondary austenite in the heat-affected zone and in the weld metal can also occur during the multi-pass welding of duplex steels when the austenite content can be significantly increased [15].

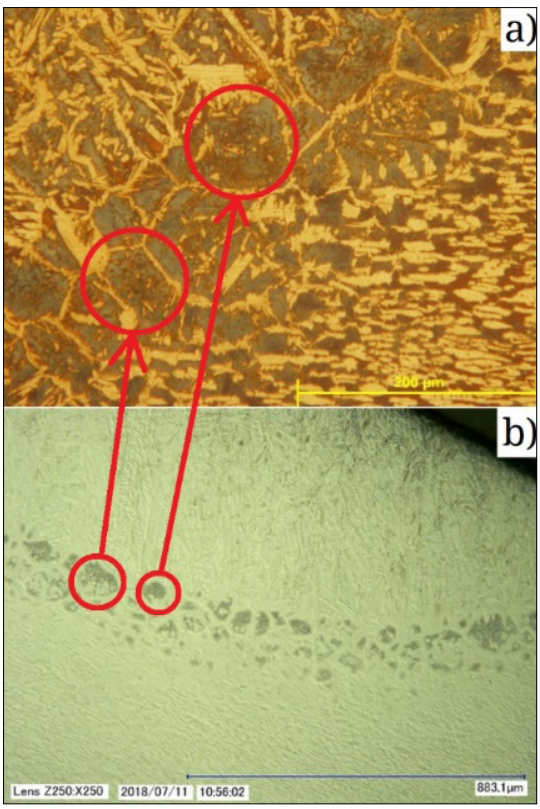

Figure 5. *Microstructure images of the heat-affected zone of the sample welded with argon shielding gas and the lowest arc energy. The relationship between secondary austenite and chromium nitride precipitates is seen in the as-welded image (b) and in the colour etching image after heat treatment (a).*

4. Conclusion

In our research, we performed TIG welding of conventional duplex steel using pure argon and nitrogen-containing shielding gases. Samples welded with pure argon were post-weld heat-treated in molten salt. The applicability of oxalic acid electrochemical etching to the detection of chromium nitride precipitates was also investigated. In addition, we investigated how these precipitates are converted to secondary austenite during heat treatment. Based on our results, it can be stated that oxalic acid electrochemical etching is a suitable method for the detection of chromium nitride precipitates. Chromium nitride precipitates were visible in the heat-affected zone, and after heat treatment, secondary austenite particles formed at the site of the nitride precipitates, which increased the austenite content of the weld metal.

Acknowledgments

The publication of the work reported herein has been supported by the NTP-SZKOLL-19-066 National Talent Programme of the Ministry of Human Capacities. “The research reported in this paper was supported by the BME Nanotechnology and Materials Science TKP2020 IE grant of NKFIH Hungary (BME IE-NAT TKP2020). The research reported in this paper was supported by the BME NC TKP2020 grant of NKFIH Hungary.

References

[1] Uzonyi S., Asztalos L., Dobránszky J.: *Duplex korrózióálló acél durvalemezek hegesztése*. Műszaki Tudományos Közlemények, 3. (2015) 315–318. https://doi.org/10.33895/mtk-2015.03.71

[2] Pálfi N., Berecz T., Fazakas É., Fábián E. R.: *Mikroszerkezeti változások 900 °C-on hőn tartott, majd alakított SAF 2507 típusú duplex korrózióálló acélban.* In OGÉT 2017: XXV. Nemzetközi Gépészeti Konferencia. 25th International Conference on Mechanical Engineering. Cluj, Románia. 2017. 303–306.

[3] Fábián E. R., Dobránszky J., Csizmazia J.: *Duplex acéllemezek lézersugaras hegesztésekor bekövetkező változások*. Műszaki tudományos közlemények, 5. (2016) 141–144. https://doi.org/10.33895/mtk-2016.05

[4] Sándor T.: *Korszerű duplex korrózióálló acélok hegeszthetőségi kérdései.* In: 25. Jubileumi Hegesztési Konferencia. Budapest, Magyarország. 2010. 19–21.

[5] Westin E. M., Johansson M. M., Pettersson R. F. A.: *Effect of nitrogen-containing shielding and backing gas on the pitting corrosion resistance of welded lean duplex stainless steel LDX 2101® (EN*

1.4162, UNS S32101). Welding in the World, 57/4. (2013) 467–476.

[6] Gunn R. N.: *Duplex stainless steels: microstructure, properties and applications*. 1. Ed., Abington Publishing, Abington, 1997. 30–41.

[7] Karlsson L.: *Welding Duplex Stainless Steels – a Review of Current Recommendations*. Welding in the World, 56/05/06. (2012) 1–17.

[8] Lőrinc Zs.: *NAS329J3L duplex acél lézersugaras felületkezelése.* In: Fiatal Műszakiak Tudományos Ülésszaka XIX. Nemzetközi Tudományos Konferencia. Kolozsvár, Románia. 2014. 277–280. https://doi.org/10.36243/fmtu-2014.0 62

[9] Bögre B., Mészáros I.: *Problems of Ferrite Content Determination.* Periodica Polytechica Mechanical Engineering, 64/2. (2020) 150–158. https://doi.org/10.3311/PPme.15022

[10] Nelson D. E., Baeslack W. A., Lippold J. C.: *Characterization of the weld structure in a duplex stainless steel using color metallography.* Metallography, 18/3. (1985) 215–225. https://doi.org/10.1016/0026-0800(85)90043-6

[11] Putz A., Hosseini V. A., Westin E. M., Enzinger N.: *Microstructure investigation of duplex stainless steel welds using arc heat treatment technique.* Welding in the World, 64. (2020) 1135–1147. https://doi.org/10.1007/s40194-020-00906-2

[12] Pettersson N., Pettersson R. F. A., Wessman S.: *Precipitation of Chromium Nitrides in the Super Duplex Stainless Steel 2507.* Metallurgical and Materials Transactions A: Physical Metallurgy and Materials Science, 46/3. (2015) 1062–1072. https://doi.org/10.1007/s11661-014-2718-y

[13] Liao J.: *Nitride precipitation in weld HAZs of a duplex stainless steel.* ISIJ International, 41/5. (2001) 460–467. https://doi.org/10.2355/isijinternational.41.460

[14] Ramirez A. J., Lippold J. C., Brandi S. D.: T*he relationship between chromium nitride and secondary austenite precipitation in duplex stainless steels*. Metallurgical and Materials Transactions A, 34/8. (2003) 1575–1597. https://doi.org/10.1007/s11661-003-0304-9

[15] Pickle T., Henry N., Morriss P., Tennis L., Wagner D., Baumer R. E.: *Root Pass Microstructure in Super Duplex Stainless Steel Multipass Welds.* Welding Journal, 98/5. (2019) 123–134. https://doi.org/ 10.29391/2019.98.010